Lattice Boltzmann simulations of a single n-butanol drop rising in water

A. E. Komrakova, D. Eskin, and J. J. Derksen

Additional information on Phys. Fluids

Lattice Boltzmann simulations of a single *n*-butanol drop rising in water

A. E. Komrakova,[1,a)] D. Eskin,[2] and J. J. Derksen[1]
[1]*Chemical and Materials Engineering, University of Alberta, 7th Floor, ECERF,*
9107 116 St., Edmonton, Alberta T6G 2V4, Canada
[2]*Schlumberger DBR Technology Center, 9450 17 Ave. NW, Edmonton,*
Alberta T6N 1M9, Canada

The motion of an *n*-butanol drop in water under the influence of gravity was numerically studied using a diffuse interface free energy lattice Boltzmann method. A pure two-liquid system without mass transfer between the phases was considered. A range of drop diameters of 1.0–4.0 mm covered the flow conditions. Most calculations were carried out in a moving reference frame. This allowed studying of long-term drop behavior in a relatively small computational domain. The capability of the method to capture the drop shape especially in the oscillating regime was demonstrated. For each drop diameter the evolution of the drop velocity in time, the terminal rise velocity and drop's shape were determined. The results were compared to experimental and numerical results and to semi-empirical correlations. The deviation of the simulated terminal velocity from other results is within 5% for smaller drops and up to 20% for large oscillating drops. It was shown that beyond the onset of shape oscillations the binary system converges towards a constant capillary number of 0.056. © *2013 AIP Publishing LLC*. [http://dx.doi.org/10.1063/1.4800230]

I. INTRODUCTION

Liquid-liquid extraction is a method for separating the components of a solution based on mass transfer.[1] The dispersion of one liquid in the form of small drops in another liquid creates large interfacial surface; thus, enhancing the mass transfer between the liquids. Even though the motion of swarms of liquid drops under the influence of net gravity through continuous liquid is frequently encountered in extraction processes,[1] a comprehensive study of single droplet behavior is the essential starting point for analysis of the process. The obtained information can be used to develop engineering models for the full extraction process.[2] The mass transfer rate, drop terminal velocity, and related drag coefficient are the crucial parameters that need to be determined.[2,3]

Experiments and numerical simulations have been utilized to understand the complex behavior of a buoyancy-driven drop moving through the ambient liquid. Accurate measurements require considerable effort.[4] As discussed by Wegener *et al.*,[3] the comparison of experimental results might be difficult because different research groups can obtain dramatically different results while seemingly investigating the same system. The authors attribute the differences mainly to the impurities in the systems. In case of numerical studies, one can fully control the purity of the system: a mathematical description of the problem can be constructed for pure or contaminated systems. However, the capability of the numerical method to capture the correct physics of the problem must be carefully checked. Only numerical results verified with reliable experimental data can be used to analyze engineering systems. In this study numerical simulations have been applied to investigate liquid drop behavior. A systematic comparison of the results with experiments has been performed.

---

a)Electronic mail: komrakov@ualberta.ca

    25, 042102-1

Early experimental studies on the motion of single liquid drops falling/rising through a stationary liquid have been reported.[5–10] The influence of walls for the settling of single organic drops through an aqueous phase was examined by Strom and Kintner.[11] The effect of surfactant on the terminal velocity of drops at small Reynolds numbers was considered by Griffith.[12] Recent experiments were performed by Dehkordi et al.,[13] who studied the sedimentation of n-butanol droplets under mass transfer conditions with and without surfactants. Transient velocity measurements of toluene droplets rising in water were carried out by Wegener et al.[3]

Bertakis et al.[4] investigated the n-butanol/water system via experiments and numerical simulations. A three-dimensional finite element technique was used. The interface was captured with the level-set approach. The drop diameters covered the range relevant to extraction processes. The authors showed spherical, deformed, and oscillating drops. Five drops with diameters spanning all mentioned flow regimes were simulated. Both experimental and numerical results were in excellent agreement with each other and with semi-empirical correlations.

Bäumler et al.[14] performed experiments and numerical simulations of three binary systems: toluene/water, n-butyl acetate/water, and n-butanol/water. A numerical approach based on the finite element method was applied. A sharp interface representation and a mesh moving method were adopted. The simulated drop terminal velocities agreed well with their experimental findings and those reported by Bertakis et al.[4] and Wegener et al.:[3] the mean deviation was below 5%. A drawback of the applied moving-mesh method was its difficulty to capture the strong drop deformations in the oscillatory regime and the inability to handle drop breakup and coalescence.

Petera and Weatherley[15] presented a two-dimensional axisymmetric method to determine the mass transfer from a deformable droplet moving in a continuous phase. A modified Lagrange-Galerkin finite element method with automatic remeshing to track the droplet shape was used. The calculated values of drop velocity and mass transfer rate were compared with experimental data determined for single drops of ethanol/water mixtures extracting into a continuous phase of n-decanol. It was shown that the method was capable of predicting the terminal velocity and the deformed droplet shape.

Watanabe and Ebihara[16] performed numerical simulations of a rising droplet using the two-component two-phase lattice Boltzmann method. The authors outlined for the single droplet that the rise velocities were in good agreement with the empirical correlation proposed by Grace et al.[17] which is valid for contaminated systems only, while the applied numerical technique was not constructed to take contaminations into account.

The commercial CFD software STAR-CD was used by Wegener et al.[18] to simulate the mass transfer across the interface of moving drops with simultaneous Marangoni convection in a fully three-dimensional problem statement. Simulations of pure toluene/water systems were performed. The terminal drop rise velocity was in good agreement with experimental data only up to 3.0 mm droplets. The applied numerical method was not able to capture deformations of larger drops.

Ohta et al.[19] presented a sensitivity study of the density and viscosity ratio on a drop moving through viscous fluid. A two-dimensional axisymmetric formulation of the coupled level-set/volume-of-fluid method with sharp interface treatment was implemented. The authors demonstrated good correlation of results using their method with several experimental cases; however, as was noted by the authors, the axisymmetric assumption might not be applicable for all physical conditions considered in the work. The essence of complex drop motion was captured, but fully three-dimensional simulations could reveal additional unstable drop behavior not observed in their work especially for oscillatory regimes.

Thus, a broad range of numerical methods has been applied to simulate single drop motion under gravity. Nevertheless, to our knowledge there are no published results where the adopted numerical approach could simulate a wide range of drop diameters handling the regions of spherical, deformed, and oscillating drops with significant topological deformations, along with the ability to model mass transfer, surfactant influence, or swarms of droplets. One of the main issues in numerical simulations of multiphase flow that might limit the method to specific problems is the description of the interface between the fluids. The interface approximation methods can be divided in two groups: interface "capturing" and "tracking" methods. The level-set,[20, 21] volume of fluid (VOF),[22, 23] phase-field,[24, 25] and lattice Boltzmann equation (LBE)[26–30] models are examples of interface capturing

methods. In these methods the interface is implicitly captured by volume functions that use the data from the same fixed grid on which the flow is calculated. The front tracking models[31–33] track the interface explicitly using a Lagrangian mesh, while the flow field is solved on a fixed Eulerian grid. Interface capturing methods are easier to implement: only one mesh is needed for the calculations. In contrast, the interface tracking models require an additional interface mesh that needs to be dynamically remeshed and mapped onto the Eulerian mesh. The drawback of the interface capturing models is that they exhibit unphysical coalescence when drops are in close proximity if no additional preventing treatments are performed, while front tracking models need a sub-grid model to allow droplets to merge or break.[34]

With special handling, as high mesh resolution, higher order schemes for discretization, and suppressed artificial coalescence most methods can give accurate results, but only for a small number of droplets in the system. When the number of droplets is increased, multiple drop interactions as coalescence and breakup should be taken into account. This requires significant computational efforts for the interface reconstruction in interface capturing methods or a proper sub-grid model in interface tracking methods.

In contrast to all multiphase methods discussed above, a diffuse interface method does not require any explicit interface treatments, as reconstruction or dynamic remeshing. The interface evolves naturally based on the thermodynamics of the model. It is assumed that the interface between two immiscible fluids has a small but finite width. Exactly this issue gives the advantage of the diffuse interface methods over the sharp interface methods because calculations are much easier for three-dimensional flows in which significant topological changes of the interface take place.[35] However, the results obtained using the diffuse interface method might not be as accurate as they could be with a sharp interface description. In the diffuse interface methods the width of the interface is deliberately enlarged to allow easier computations, while in real physical systems the interface is extremely thin. Thus, to properly and accurately model relevant physical phenomena, the interface thickness must be taken as small as possible which is not always an easy task in terms of numerical stability. On the positive side, diffuse interface methods provide the possibility to run simulations of large-scale three-dimensional systems with multiple interacting droplets.

In this study the motion of an organic *n*-butanol drop in water under the influence of gravity is simulated using a diffuse interface free energy LBE technique originally proposed by Swift *et al.*[29] (see Ref. 36 for a general LBE description). This method is not widely used for complex flow modeling yet; thus, one of the major goals of the present work is to investigate its capabilities of liquid/liquid flow simulations. The LBE models operate in so-called lattice space, where all physical parameters are expressed in lattice units. It is shown in the current paper that all essential physical parameters of the investigated system can be matched with the corresponding parameters in the lattice space. The numerical results obtained in this study are compared in great detail to the experimental and numerical results reported by Bertakis *et al.*[4] and Bäumler *et al.*[14] A wide range of drop diameters is considered to show the ability of the method to capture the drop shape deformation especially in the oscillating regime. Thus, the application of a trustworthy simulation approach, able to reveal the required flow details with reasonable computational cost is the aim of the present study.

The rest of the paper is organized as follows: Section II outlines the exact problem statement. The governing equations, the numerical method to solve these equations, the moving frame implementation, and the scaling procedure are shown in Sec. III. Section IV contains the verification of the applied numerical method. The main results and comparison with experimental data are presented in Sec. V. Finally, the main findings of this work are summarized in Sec. VI.

II. PROBLEM STATEMENT

Numerical simulation of a single *n*-butanol drop moving through water under the influence of gravity is the focus of the present study. The computational setup mimics the experimental conditions described by Bertakis *et al.*[4] A sedimentation apparatus was used in the experiments: the droplets were generated through a nozzle into a cylindrical cell that contained the continuous phase. The dimensions of the cell (hight 500 mm and diameter 40 mm) were significantly larger compared to the drop diameters (4.0 mm and less) to minimize wall confinement effects. After generation, the

TABLE I. Physical parameters of the *n*-butanol/water binary system.[4]

Liquids	Density (kg/m^3)	Dynamic viscosity (mPa s)	Surface tension (mN/m)
n-butanol	$\rho_d = 845.1$	$\mu_d = 3.28$	$\sigma = 1.63$
Water	$\rho_c = 986.5$	$\mu_c = 1.39$	

droplets were given about 12 cm of acceleration distance to reach terminal velocity. Drops positions were monitored using a camera recording 30 frames per second. The droplet travel time for the given distance was calculated as the number of frames recorded from the time the drop enters the measuring region to the time of exit. The drop terminal rise velocity was calculated from these data. As outlined by Bertakis *et al.*,[4] the organic and aqueous phases were mutually saturated to avoid mass transfer. A precise cleaning procedure of experimental equipment was accomplished; deionized and distilled water and only chemicals of high purity were used. The computational approach applied in the present numerical study is constructed for binary liquid systems only; there are no surfactants or contaminations. The purity of the experimental system allows comparison of experimental results to those obtained using our proposed numerical procedure. The mass transfer between the two liquids was avoided in the experiments; thus, it is not modeled in the present investigation. The physical parameters of the system are shown in Table I.

The motion of drops in ambient liquid has two effects that distinguish it from solid particle motion: the mobility of the interface and the ability of a drop to change its shape. When the drop is driven by gravity the following parameters define the physics of the flow:

$$u = f(d, \ \rho_c, \ \rho_d, \ \mu_c, \ \mu_d, \ \sigma, \ g) \tag{1}$$

here the subscripts *d* and *c* stand for the dispersed and continuous phase, respectively; $d = (6V/\pi)^{1/3}$ is the volume-equivalent diameter of the drop, *V* is the drop volume; ρ_c and ρ_d are the densities and $\Delta\rho = \rho_c - \rho_d$ is the density difference; μ_c and μ_d are the dynamic viscosities; σ is the surface tension; *g* is the gravitational acceleration.

The system of these parameters gives five independent dimensionless numbers that fully determine the problem: the Reynolds number $\mathrm{Re} = ud\rho_c/\mu_c$ (where *u* is the drop terminal velocity); the Weber number $\mathrm{We} = \rho_c u^2 d/\sigma$; the Froude number $\mathrm{Fr} = u^2/(gd)$; the density ratio $\lambda = \rho_d/\rho_c$; and the dynamic viscosity ratio $\eta = \mu_d/\mu_c$.

Clift *et al.*[37] organized the shapes and terminal velocities of the drops and bubbles based on the Reynolds, Eötvös (Eo) and Morton (Mo) numbers. The two latter ones are defined as

$$\mathrm{Eo} = \frac{g\Delta\rho d^2}{\sigma} = \frac{\mathrm{We}|1-\lambda|}{\mathrm{Fr}}, \tag{2}$$

$$\mathrm{Mo} = \frac{g\Delta\rho \nu_c^4 \rho_c^2}{\sigma^3} = \frac{\mathrm{We}^2\mathrm{Eo}}{\mathrm{Re}^4}. \tag{3}$$

The Eötvös number is the ratio of the buoyancy over interfacial tension. The Morton number characterizes the physical properties of the liquids and is constant for the given binary system. The effect of three dimensionless numbers $\mathrm{Re} - \mathrm{Eo} - \mathrm{Mo}$ on the shape of a drop/bubble moving through the liquid due to gravity is represented by a plot of Reynolds number against Eötvös number for different Morton numbers. This diagram of Clift *et al.*[37] is considered a standard reference for predicting the shape and velocity of fluid particles.

III. NUMERICAL METHOD

A. Governing equations

In diffuse interface (or phase field) models[24,38,39] the sharp interface between the fluids is represented by a thin transition region with finite thickness where fluids may mix. The main idea of the phase field model is that the state of the system at any given time can be described by the order

parameter of the phase field ϕ which is a function of the position vector $\boldsymbol{r}$ and time t.[40] Being mostly uniform in the bulk phases, the ϕ parameter varies continuously over the thin interfacial regions.[25] If the phase field is used to describe the binary mixture behavior, the order parameter has a physical meaning: for an isothermal binary fluid (as in this study) ϕ is the relative concentration of the two components.[25,41] To simulate the fluid dynamics of the binary mixture of two fluids, the continuity and momentum equations are used in conjunction with the convection-diffusion equation for the order parameter as proposed by Cahn-Hilliard.[41,42]

To describe quantitatively the binary system even when it is not in equilibrium state, a Helmholtz free energy written as a functional of ϕ can be used.[40] The following form of the free energy functional is adopted in the present numerical model[41,43] (the Einstein summation convention has been used),

$$\mathscr{F}(\phi) = \int \left[\mathscr{V}(\phi) + \frac{\kappa}{2}\left(\partial_\alpha \phi\right)^2 \right] d\boldsymbol{r}. \tag{4}$$

Here, $\mathscr{V}(\phi)$ is the bulk energy density which has a double-well structure with two minima corresponding to the two stable phases of the fluid. The term $\frac{\kappa}{2}(\partial_\alpha\phi)^2$ accounts for the surface energy, with κ a positive constant.

The variation in $\mathscr{F}$ for a small local variation in composition is described by the chemical potential μ,

$$\mu(\phi) \equiv \frac{\delta\mathscr{F}(\phi)}{\delta\phi} = \frac{d\mathscr{V}}{d\phi} - \kappa\partial^2_{\alpha\alpha}\phi. \tag{5}$$

For a system with fixed volume and temperature, the equilibrium state refers to the minima of the functional $\mathscr{F}(\phi)$ with respect to variations of the ϕ function,[24] i.e., $\mu(\phi) = 0$. The evolution equation of ϕ is a nonlinear convection-diffusion equation of the following form:[29,41–43]

$$\partial_t\phi + \partial_\alpha(\phi u_\alpha) = M\partial^2_{\beta\beta}\mu, \tag{6}$$

where u_α is the velocity field and M is an order parameter mobility that controls the strength of the diffusion. The order parameter diffuses due to the composition gradients and is advected by the fluid flow.[44]

To simulate the two-phase flow, Eq. (6) has to be coupled with the Navier-Stokes equation. The non-uniformity of the composition causes a thermodynamic force density $-\phi\partial_\alpha\mu$ that acts at each point in the fluid[44] (the chemical potential gradient pulls the two species in opposite directions). If $\phi = 0$ the net force vanishes. As an alternative way this thermodynamic force density can be introduced as the divergence of a "chemical" pressure tensor

$$\phi\partial_\alpha\mu = \partial_\alpha P^{chem}_{\alpha\beta}, \tag{7}$$

where the "chemical" pressure tensor[44] is given by

$$P^{chem}_{\alpha\beta} = \delta_{\alpha\beta}\left[\phi\frac{\delta\mathscr{V}}{\delta\phi} - \mathscr{V} - \kappa\{\phi\partial^2_{\gamma\gamma}\phi + \frac{1}{2}|\partial_\alpha\phi|^2\}\right] + \kappa(\partial_\alpha\phi)(\partial_\beta\phi). \tag{8}$$

Thus, the order parameter influence can be incorporated into the Navier-Stokes equation in two ways: either by introduction of the term $-\partial_\alpha P^{chem}_{\alpha\beta}$ or by a body force density $-\phi\partial_\alpha\mu$. In the present study, the order parameter was taken into account using the first approach.

Complex morphological and topological flow transitions such as coalescence and interface breakup are captured naturally in the free energy based multiphase models. Moreover, different phenomena can be accounted for in the model by a suitable modification of the free energy functional. The main drawback is that to properly model relevant physics, the interface layers have to be thin.[25] This issue causes large gradients of the phase field in the interface region which must be resolved computationally.

Finally, the mathematical description of the binary mixture at constant temperature can be formulated. The evolution of density, velocity, and concentration fields is governed by the continuity,
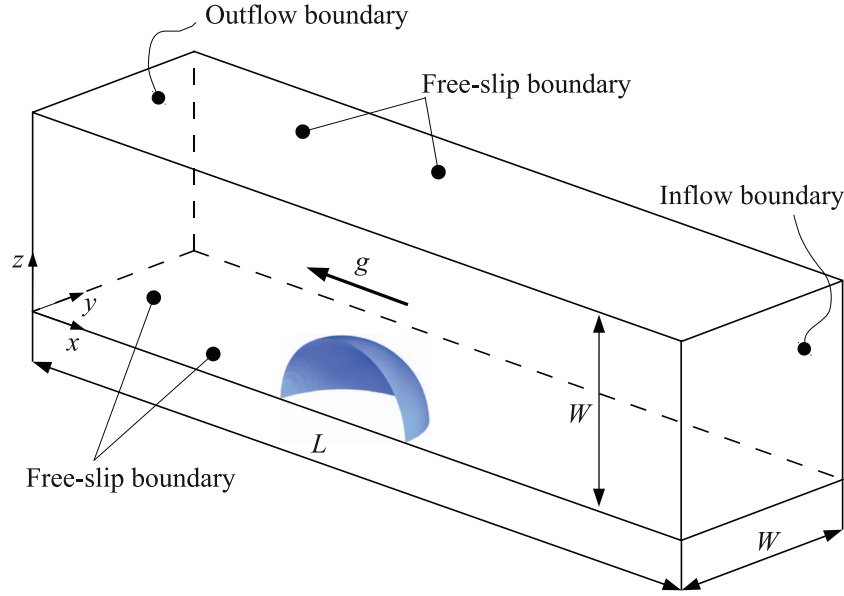
FIG. 1. Simulation domain with boundary conditions: $x = 0$ is the outflow boundary; $x = L$ is the inflow boundary; all the rest side boundaries are the free-slip walls. The drop is kept in the middle of the simulation domain and has a spherical shape at $t = 0$.

momentum and convection-diffusion equations,[29, 44, 45] respectively,

$$\partial_t \rho + \partial_\alpha (\rho u_\alpha) = 0, \tag{9a}$$

$$\partial_t(\rho u_\alpha) + \partial_\beta(\rho u_\alpha u_\beta) = -\partial_\beta P_{\alpha\beta}^{th} + \partial_\beta \nu \left(\rho \partial_\alpha u_\beta + \rho \partial_\beta u_\alpha \right) + g_\alpha \Delta \rho - \rho a_{F\alpha}, \tag{9b}$$

$$\partial_t \phi + \partial_\alpha (\phi u_\alpha) = M \partial_{\beta\beta}^2 \mu, \tag{9c}$$

where ρ is the density of the mixture; and ν is the shear viscosity. Here $P_{\alpha\beta}^{th}$ is the "thermodynamic" pressure tensor. It contains two parts:[44] an isotropic contribution $P\delta_{\alpha\beta}$ that represents the ideal gas pressure and the "chemical" pressure tensor $P_{\alpha\beta}^{chem}$ defined by Eq. (8). The isotropic contribution to the pressure tensor as well as the explicit form of $\mathscr{V}$ are discussed in Sec. III B.

This model can be used only for density-matched fluids. Since the relative density difference of the considered liquids is 14%, the Boussinesq approximation has been adopted for determining the net gravity forces. The buoyancy force on the dispersed drop is taken into account by introduction of the net force acting on the drop: the term $g_\alpha \Delta \rho$ in momentum equation (9b).

With the intent to limit the computational resources while studying the long-term evolution of the drops, the moving frame technique has been adopted (see Sec. III D for details). In addition, all drops considered in the present simulations rise vertically; therefore, due to the symmetry of the flow, only a quarter of the drop is considered. The simulation domain is depicted in Fig. 1. Initially a spherical droplet is placed in the center of the domain. For an external observer, the drop is at rest while the non-inertial coordinate system is accelerated opposite to the inlet flow. The acceleration of the reference frame $\boldsymbol{a}_F$ has been accounted for in the momentum equation (9b) by the term $\rho a_{F\alpha}$.

B. LBE method implementation

The system of Eqs. (9) that governs the binary system behavior can be solved using different numerical techniques. Swift et al.[29] developed a lattice Boltzmann approach, known as free energy model, to solve the system. This method is adopted in the present study. Two particle distribution

functions are utilized: one function $f(\boldsymbol{r}, t)$ is used to solve the continuity (9a) and the Navier-Stokes (9b) equations and the second one $g(\boldsymbol{r}, t)$ is used for the convection-diffusion equation (9c). The distribution functions evolve with discrete time steps Δt. Analysis of preliminary results showed that with the set of numerical parameters representing the given physical system, a two-relaxation-time (TRT) collision operator[46] should be used to increase accuracy and improve stability. The fully discretized lattice Boltzmann equations have the following form:

$$f_q(\boldsymbol{r} + \boldsymbol{c}_q \Delta t, t + \Delta t) = f_q(\boldsymbol{r}, t) + \lambda^{\mathrm{sf}}\Big(f_q^{\mathrm{s}}(\boldsymbol{r}, t) - f_q^{\mathrm{seq}}(\boldsymbol{r}, t)\Big)$$

$$+ \lambda^{\mathrm{af}}\Big(f_q^{\mathrm{a}}(\boldsymbol{r}, t) - f_q^{\mathrm{aeq}}(\boldsymbol{r}, t)\Big) + F_q,$$

$$g_q(\boldsymbol{r} + \boldsymbol{c}_q \Delta t, t + \Delta t) = g_q(\boldsymbol{r}, t) + \lambda^{\mathrm{sg}}\Big(g_q^{\mathrm{s}}(\boldsymbol{r}, t) - g_q^{\mathrm{seq}}(\boldsymbol{r}, t)\Big)$$

$$+ \lambda^{\mathrm{ag}}\Big(g_q^{\mathrm{a}}(\boldsymbol{r}, t) - g_q^{\mathrm{aeq}}(\boldsymbol{r}, t)\Big), \tag{10}$$

where the index q stands for the number of the velocity direction (each velocity vector has an opposite one); bold symbols stand for vectors; $\boldsymbol{c}_q$ denotes the discrete velocity set, with the magnitude defined as $c = \Delta x / \Delta t$ (Δx is the mesh step); $f_q(\boldsymbol{r} + \boldsymbol{c}_q \Delta t, t + \Delta t)$ and $g_q(\boldsymbol{r} + \boldsymbol{c}_q \Delta t, t + \Delta t)$ represent the post-collision particle distribution function at $(\boldsymbol{r}, t)$ streamed to the neighboring nodes located at $(\boldsymbol{r} + \boldsymbol{c}_q \Delta t)$ and at time $t + \Delta t$ along direction q; $f_q(\boldsymbol{r}, t)$ and $g_q(\boldsymbol{r}, t)$ are the pre-collision particle distribution function; $f_q^{\mathrm{s}}, g_q^{\mathrm{s}}$ and $f_q^{\mathrm{seq}}, g_q^{\mathrm{seq}}$ are the symmetric parts of the particle distribution function and equilibrium distribution function, respectively; $f_q^{\mathrm{a}}, g_q^{\mathrm{a}}$ and $f_q^{\mathrm{aeq}}, g_q^{\mathrm{aeq}}$ are the anti-symmetric parts of the particle distribution function and equilibrium distribution function, respectively; $\lambda^{\mathrm{sf}}, \lambda^{\mathrm{sg}}$ and $\lambda^{\mathrm{af}}, \lambda^{\mathrm{ag}}$ are the symmetric and anti-symmetric collision rates for f and g populations, respectively; F_q is the forcing term.

In the TRT collision operator, particle distribution functions are relaxed to the equilibrium state by relaxing their symmetric and anti-symmetric parts separately, which are given by

$$f_q^{\mathrm{s}} = \frac{f_q + \overline{f_q}}{2} \qquad\qquad f_q^{\mathrm{a}} = \frac{f_q - \overline{f_q}}{2}$$

$$f_q^{\mathrm{seq}} = \frac{f_q^{\mathrm{eq}} + \overline{f_q^{\mathrm{eq}}}}{2} \qquad\qquad f_q^{\mathrm{aeq}} = \frac{f_q^{\mathrm{eq}} - \overline{f_q^{\mathrm{eq}}}}{2}, \tag{11}$$

where f_q^{eq} is Maxwellian-Boltzmann distributions (or equilibrium distributions); $\overline{f_q}$ and $\overline{f_q^{\mathrm{eq}}}$ are the particle distribution functions and equilibrium distribution function in the direction opposite of q. The same set of equations can be written for the particle distribution function g.

The D3Q19 lattice (see the Appendix) is adopted here. In this lattice arrangement, each site communicates with six nearest and 12 diagonal neighbors. Only a uniform cubic lattice can be used; the mesh step Δx is taken as unity, as is the time step Δt.

The particle distribution functions are defined such that the following summations over all directions q, at a single lattice point gives the local density of the fluid, local fluid momentum and local order parameter, respectively,

$$\sum_q f_q = \rho \qquad \sum_q \boldsymbol{c}_q f_q = \rho \boldsymbol{u} + \frac{\Delta t}{2} \boldsymbol{F} \qquad \sum_q g_q = \phi. \tag{12}$$

The forcing term is incorporated as follows:

$$F_q = w_q (\boldsymbol{c}_q \cdot \boldsymbol{F}), \tag{13}$$

where $\boldsymbol{F}$ is the macroscopic force and w_q are the weight coefficients presented in the Appendix.

The full pressure tensor $P_{\alpha\beta}$ is given by

$$P_{\alpha\beta} = \sum_q f_q c_{q\alpha} c_{q\beta}. \tag{14}$$

The equilibrium distributions can be derived from conditions (12) along with the condition that the order parameter is advected by the fluid

$$\sum_q g_q^{eq} e_{q\alpha} = \phi u_\alpha, \tag{15}$$

and that the pressure tensor and chemical potential at equilibrium obey

$$\sum_q f_q^{eq} e_{q\alpha} e_{q\beta} = P_{\alpha\beta}^{th} + \rho u_\alpha u_\beta,$$

$$\sum_q g_q^{eq} e_{q\alpha} e_{q\beta} = \Gamma \mu \delta_{\alpha\beta} + \phi u_\alpha u_\beta. \tag{16}$$

The equilibrium distributions[47] are presented in the Appendix.

The two liquids have different kinematic viscosities. To take this into account, the kinematic viscosity of the mixture ν is set to be a linear function of the order parameter ϕ,

$$\nu(\phi) = \nu_c \frac{1-\phi}{2} + \nu_d \frac{1+\phi}{2}, \tag{17}$$

where ν_c and ν_d are the kinematic viscosities of continuous and dispersed phases, respectively.

Then the relaxation parameter for f is defined using the kinematic viscosity of the mixture

$$\tau_f = \frac{\nu}{c_s^2 \Delta t} + \frac{1}{2}, \tag{18}$$

where $c_s^2 = 1/3$ is the speed of sound in lattice space.

The mobility M, the coefficient of mobility Γ, and the relaxation parameter τ_g are connected by the following relation:[29]

$$M = \Delta t \Gamma \left(\tau_g - \frac{1}{2} \right). \tag{19}$$

The symmetric collision rate for the f distribution function λ^{sf} is fixed by the kinematic viscosity of the fluid using the relation $\lambda^{sf} = -1/\tau_f$. The symmetric eigenvalue function is calculated as follows:

$$\Lambda^{sf} = -\left(\frac{1}{2} + \frac{1}{\lambda^{sf}} \right). \tag{20}$$

The symmetric and anti-symmetric functions[46] are related by the "magic" parameter Λ_{eo}^f,

$$\Lambda_{eo}^f = \Lambda^{sf} \Lambda^{af}. \tag{21}$$

If the "magic" parameter is fixed, then the anti-symmetric eigenvalue function can be calculated as $\Lambda_a^f = \Lambda_{eo}^f / \Lambda_s^f$. The anti-symmetric collision rate is then defined as

$$\lambda^{af} = -\frac{1}{\Lambda^{af} + \frac{1}{2}}. \tag{22}$$

The parameters for the g distribution function are determined in a similar way. The symmetric collision rate λ^{sg} is defined using the relaxation time τ_g as follows $\lambda^{sg} = -1/\tau_g$. All steps for determining λ^{ag} remain the same provided the "magic" parameter for the g distribution function Λ_{eo}^g is given.

In this study, the following form of the free energy functional is used:[44,48]

$$\mathscr{F}[\phi, \rho] = \int \left[c_s^2 \rho \ln \rho + \mathscr{V} + \frac{\kappa}{2} (\partial_\alpha \phi)^2 \right] d\boldsymbol{r}. \tag{23}$$

The ideal gas pressure $p_{id} = \rho T$ is incorporated via the first term in expression (23), and it does not affect the phase behavior. A symmetrical double well potential is utilized to describe the phase

separation

$$\mathscr{V} = \frac{A}{2}\phi^2 + \frac{B}{4}\phi^4, \tag{24}$$

where $A < 0$ and B determine the properties of the bulk phases.

The chemical potential thus reads

$$\mu(\phi) = A\phi + B\phi^3 - \kappa\partial_{\alpha\alpha}^2\phi. \tag{25}$$

The analytical solution for the planar interface[49] is

$$\phi(x) = \phi_0 \tanh(x/\xi). \tag{26}$$

Here, $\phi = \pm\phi_0$ is the value of order parameter in the bulk phase at either side of the interface, and follows from Eq. (25),

$$\phi_0 = \left(\frac{A}{B}\right)^{1/2}. \tag{27}$$

It is assumed that $A = B$ which means $\phi_0 = 1$.

The thickness of the diffuse interface ξ is equal to

$$\xi = \left(\frac{2\kappa}{A}\right)^{1/2}. \tag{28}$$

The surface tension σ follows from

$$\sigma = \frac{4}{3}\kappa\frac{\phi_0^2}{\xi}. \tag{29}$$

An important addition to (23) is the term dependent on density ρ, here chosen as an "ideal gas" type contribution. This gives a diagonal term in the thermodynamic pressure tensor, which becomes

$$P_{\alpha\beta}^{th} = \left[c_s^2\rho + \frac{A}{2}\phi^2 + \frac{3B}{4}\phi^4 - \kappa\phi\partial_{\alpha\alpha}^2\phi - \frac{1}{2}|\partial_\alpha\phi|^2\right]\delta_{\alpha\beta} + \kappa(\partial_\alpha\phi)(\partial_\beta\phi), \tag{30}$$

so that the thermodynamic stress obeys $P_{\alpha\beta}^{th} = c_s^2\rho\delta_{\alpha\beta} + P_{\alpha\beta}^{chem}$.

To determine the pressure tensor, the spatial gradients of ϕ have to be calculated. The stencils for gradients and Laplacian calculations adopted in this study are given in the Appendix.

The discretized equations (10) are solved in two steps:

$$\text{Collision step: } f_q'(\boldsymbol{r}, t) = f_q(\boldsymbol{r}, t) + \lambda^{\text{sf}}(f_q^s - f_q^{\text{seq}}) + \lambda^{\text{af}}(f_q^s - f_q^{\text{aeq}}) + F_q$$
$$g_q'(\boldsymbol{r}, t) = g_q(\boldsymbol{r}, t) + \lambda^{\text{sg}}(g_q^s - g_q^{\text{seq}}) + \lambda^{\text{ag}}(g_q^s - g_q^{\text{aeq}}), \tag{31}$$

$$\text{Streaming step: } f_q(\boldsymbol{r} + \boldsymbol{c}_q\Delta t, t + \Delta t) = f_q'(\mathbf{r}, t)$$
$$g_q(\boldsymbol{r} + \boldsymbol{c}_q\Delta t, t + \Delta t) = g_q'(\mathbf{r}, t). \tag{32}$$

To complete the mathematical problem statement, boundary conditions have to be specified. Since the LBE method deals with particle distribution functions instead of general hydrodynamic variables, one should apply boundary conditions for the distribution functions such that boundary conditions for the hydrodynamic variables are met.

The solution of the problem in the moving reference frame requires inflow and outflow boundary conditions. At the inlet $x = L$ (Fig. 1), a uniform velocity is imposed. At the outlet $x = 0$, a constant pressure boundary condition corresponding to $\rho = 1$ is used. These boundary conditions for velocity $\boldsymbol{u}$ and pressure p can be set using the procedures proposed by Mussa et al.[50] For the second distribution function g the periodic boundary condition is imposed on the inflow/outflow faces. On

all side walls the free-slip condition for both distribution functions is applied. This type of boundary treatment can be handled by specular reflection[51] of f and g.

C. Scaling procedure

The lattice Boltzmann method operates in so-called lattice space, and all system parameters are presented in lattice units [lu]. Thus, it is very important to correctly match the parameters of the physical system (in physical units) with the numerical system in lattice units. The physical system translation into lattice space is performed using scaling factors. The scaling factor is the ratio of any parameter value in physical units to the corresponding parameter in lattice units. To obtain the values of these scaling factors it is necessary to equate the essential dimensionless parameters defined in physical and lattice space. Further in this section, the symbols with a tilde stand for parameters in lattice units.

By definition, the scaling factor for surface tension reads $C_\sigma = \sigma/\widetilde{\sigma}$. Two numerical parameters related to the free energy model and particularly to surface tension, κ and A, have to be determined. The expression for κ is derived from Eq. (29) and reads

$$\kappa = \frac{3\xi}{4\phi_0^2}\frac{\sigma}{C_\sigma}. \tag{33}$$

In this study the interface width ξ was fixed to 1.14 [lu] for all cases (based on the results reported by Kendon *et al.*[44]). Once κ is determined the value of A is calculated using Eq. (28).

For the adopted LBE model, the value of the density in the incompressible limit should be equal to unity. Thus, the continuous phase density in lattice space is set to $\widetilde{\rho}_c = 1$. The dispersed phase density is defined by the density ratio $\widetilde{\rho}_d = \lambda\widetilde{\rho}_c$.

The Boussinesq approximation states that if the density difference is small compared to the actual density of the liquids, density variations are only important in the forcing term $\Delta\rho\boldsymbol{g}$ for the present problem. The proper scaling of forcing should be performed. Using the definition of the Eötvös number the forcing term reads

$$\widetilde{\Delta\rho g} = \frac{\widetilde{\sigma}}{\widetilde{d}^2}\text{Eo}, \tag{34}$$

where $\widetilde{d}$ is the drop diameter in lattice units.

Utilizing the definition of the Morton number and given the viscosity ratio η, the dynamic viscosities of continuous $\widetilde{\mu}_c$ and dispersed $\widetilde{\mu}_d$ phases are calculated

$$\widetilde{\mu}_c = \left(\widetilde{\rho}_c^2\widetilde{\sigma}^2\widetilde{d}^2\frac{\text{Mo}}{\text{Eo}}\right)^{1/4} \qquad \widetilde{\mu}_d = \eta\widetilde{\mu}_c. \tag{35}$$

The kinematic viscosities of the phases are $\widetilde{\nu}_c = \widetilde{\mu}_c/\widetilde{\rho}_c$, $\widetilde{\nu}_d = \widetilde{\mu}_d/\widetilde{\rho}_d$.

The relaxation parameters corresponding to both phases are given by

$$\tau_c = \frac{\widetilde{\nu}_c}{c_s^2\Delta t} + \frac{1}{2} \qquad \tau_d = \frac{\widetilde{\nu}_d}{c_s^2\Delta t} + \frac{1}{2}. \tag{36}$$

Therefore, the following scale factors are introduced:

Surface tension scale, N/m: $C_\sigma = \sigma/\widetilde{\sigma}$

Density scale, kg/m^3: $C_\rho = \rho/\widetilde{\rho}$

Kinematic viscosity scale, m^2/s: $C_\nu = \nu_c/\widetilde{\nu}_c$ $\qquad$ (37)

Forcing scale, N/m^3: $C_{\text{force}} = \Delta\rho g/\widetilde{\Delta\rho g}$.

TABLE II. Drop diameter d and corresponding Eötvös number Eo considered in the present simulations.

d (mm)	Eo	d (mm)	Eo
1.0	0.85	2.26	4.34
1.2	1.22	2.48	5.22
1.4	1.66	2.6	5.74
1.5	1.91	2.8	6.66
1.56	2.07	3.0	7.64
1.79	2.72	3.2	8.69
1.8	2.75	3.48	10.28
1.9	3.06	3.6	11.00
2.0	3.39	3.8	12.26
2.12	3.82	4.0	13.58

Using the definitions of Froude, Reynolds, and Weber numbers and utilizing the scaling factors (37) the values of velocity, length, and time scaling factors, are defined as follows:

$$\text{Length scale, m: } C_d = C_\nu^2 C_\rho / C_\sigma$$

$$\text{Velocity scale, m/s: } C_u = C_\sigma / (C_\nu C_\rho) \tag{38}$$

$$\text{Time scale, s: } C_t = C_\nu^3 C_\rho^2 / C_\sigma^2.$$

With the use of scaling factors (37) and (38) all parameters of the system in physical space are translated to the lattice space.

The dimensionless numbers that define the problem can be divided in two groups: the input dimensionless numbers that are based on input parameters and do not contain the resulting terminal drop velocity (Eo, Mo, λ, η), and output dimensionless numbers (Re, We, Fr) that can be calculated only when the drop velocity is known. Thus, in the present study for the given binary liquid system (*n*-butanol/water) with density ratio $\lambda = 0.86$, dynamic viscosity ratio $\eta = 2.36$ and the Morton number Mo $= 1.23 \times 10^{-6}$ the range of Eo numbers that corresponds to different drop diameters being considered is listed in Table II.

To perform simulations that capture the physics of the problem, the input dimensionless numbers defined in physical and lattice spaces should be matched. With the proposed scaling procedure, the forcing term (34) and phase viscosities (35) depend on the drop diameter $\widetilde{d}$. This means that the input parameters in lattice space are not unique. The simulation results obtained using different sets of input parameters all having the same Eo, Mo, λ, η will not be precisely the same. There are three main factors that determine the choice of numerical parameters and, consequently, influence the results: accuracy, stability, and compressibility effects. The results of several test problems helped to define the proper set of input parameters in lattice space. First of all, the simulation results have to satisfy the incompressibility limit, i.e., the terminal drop velocity in lattice units should be not more than $0.1c_s$. If the resulting velocity of the drop does not fulfill this inequality, then the chosen set of parameters cannot be used. This criterion was used as the first filter to "sort" the proper numerical parameters.

The choice of the drop diameter in lattice units $\widetilde{d}$ defines the spatial resolution and, thus, has a significant effect on the accuracy of the results and the computational effort. A proper balance between resolution and simulation time should be found. A drop diameter of 30–40 [lu] to represent the smallest drop of 1.0 mm gives small values of the phase viscosities in lattice space. This leads to relaxation parameters τ_c and τ_d close to 0.5. Such small values of the relaxation times for the flow field cause numerical instability. Moreover, together with a low surface tension value, they limit the range of τ_g values for which the simulation remains stable. To improve the stability and gain the accuracy the TRT collision operator has been adopted.
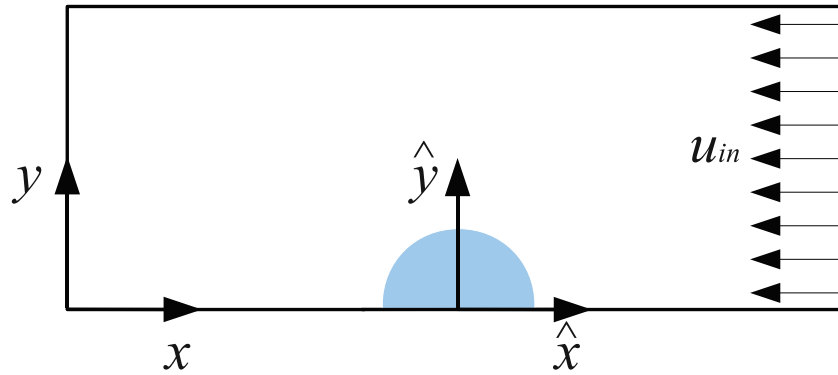
FIG. 2. Simulation domain slice ($z = 0$). Inertial (stationary) reference frame (x-y); non-inertial (moving) reference frame ($\hat{x}$-$\hat{y}$).

In order to make the proper choice of $\widetilde{\sigma}$, a benchmark problem is needed to verify the numerical results. This validation gives strong evidence that the numerical model produces physically correct results.

In the present study, the drop diameter in lattice units $\widetilde{d}$ that represents a 1.0 mm drop is fixed to 30 [lu]. Also it was found during test simulations that the value of the surface tension scaling factor should be $C_\sigma = 1.0$ N/m. This choice of parameters gives a continuous phase kinematic viscosity of $\widetilde{\nu}_c = 7.67 \times 10^{-3}$, the linear dimension scale factor, or the mesh step, $C_d = 3.33 \times 10^{-5}$ m and time scale factor, or the time step, $C_t = 6.04 \times 10^{-6}$ s. This set of parameters is our base set. The accuracy of the results obtained using this base set is discussed in Sec. IV B. The diameters $\widetilde{d}$ of the larger drops are determined in a such way as to keep the kinematic viscosity of the continuous phase constant and equal to 7.67×10^{-3}.

To check the mesh convergence or possibility to coarsen the mesh, it is necessary to rescale the parameters. The idea of mesh refinement is to increase the drop diameter $\widetilde{d}$ f_m times ($\widetilde{d}_2 = f_m \widetilde{d}_1$, $f_m > 1.0$) while keeping all dimensionless numbers and liquid viscosities the same $\widetilde{\mu}_{c2} = \widetilde{\mu}_{c1}$, $\widetilde{\mu}_{d2} = \widetilde{\mu}_{d1}$. The same idea applies to mesh coarsening, but the drop diameter is reduced in $0 < f_m < 1$ times. The interface thickness remains the same ($\xi_2 = \xi_1$). To rescale the simulation parameters it is necessary to equate the Eötvös and Morton numbers for the fine and coarse drops. The following relations are obtained:

$$\frac{\widetilde{\sigma}_2}{\widetilde{\sigma}_1} = \frac{1}{f_m} \qquad \frac{(\widetilde{\Delta\rho g})_2}{(\widetilde{\Delta\rho g})_1} = \frac{1}{f_m^3} \qquad \frac{\kappa_2}{\kappa_1} = \frac{1}{f_m} \qquad \frac{A_2}{A_1} = \frac{1}{f_m}. \tag{39}$$

The results of the mesh convergence study are discussed in Sec. IV B.

D. Moving reference frame

The larger the droplet diameter the longer distance it should travel to reach steady-state. Long computational domains can be avoided if the problem is solved in a moving reference frame. The idea is to move the computational domain along with the drop and keep the drop centered within the domain by adjusting the velocity of the frame. The implementation of the moving frame has been done in the same manner as presented by Rusche.[52]

The drop moves with respect to the stationary (inertial) reference frame (x-y), but remains centered within the moving (non-inertial) reference frame ($\hat{x}$-$\hat{y}$) (see Fig. 2). Every time step the velocity of the moving reference frame v_F is corrected as follows:

$$v_F = v_F^o + \Delta v_F, \tag{40}$$

where v_F^o is the velocity of the reference frame at the previous (old) time step. The negative value of the moving frame velocity is imposed as the inlet boundary condition $u_{in} = -v_F$.

The correction for the velocity Δv_F is calculated using the following expression:[52]

$$\Delta v_F = \lambda_f \frac{\widehat{x}_d^f - \widehat{x}_d}{\Delta t} - \lambda_o \frac{\widehat{x}_d - \widehat{x}_d^o}{\Delta t}, \qquad (41)$$

where Δt is the time step and $\widehat{x}_d$ is the center of mass of the drop relative to the moving reference frame; the superscripts f and o denote values at the first ($t = 0$) and the previous time step. The λ_f and λ_o are under-relaxation factors. The center of mass of the drop relative to the moving frame is calculated as follows:

$$\widehat{x}_d = \frac{\sum \phi \widehat{x}}{\sum \phi}, \qquad (42)$$

where the summation is performed over all positive ϕ; it is assumed that the drop is represented only by positive order parameter value ($\phi = 0$ represents the interface).

As discussed by Rusche,[52] the first term in Eq. (41) is the velocity sufficient to translate the drop back to its original position in the moving frame of reference within a single time step. The second term represents the drop velocity relative to the moving reference frame. The purpose of the second term is to avoid overshoots that appear as a result of the first term's corrections: these corrections accumulate until the drop reaches its original position. To damp both terms, under-relaxation factors λ_f and λ_o are used. It was outlined by Rusche[52] that $\lambda_f = \lambda_o = 0.1$ yields good results. In the present study the same values have been used.

To account for the time-dependent motion of the domain an extra acceleration term is added to the momentum equation (9b). To obtain the value of moving reference frame acceleration, the time derivative of the frame velocity has to be determined as follows:

$$a_F = -\frac{\Delta v_F}{\Delta t}. \qquad (43)$$

The velocity of the drop in a stationary reference frame u is calculated as the sum of the volume-averaged drop velocity in the moving reference frame and the velocity of the moving frame v_F.

IV. NUMERICAL TECHNIQUE VERIFICATION

A computer code for three-dimensional simulations has been developed using FORTRAN 90 in both serial and parallel versions. The parallel code uses domain decomposition and the MPI (message passing interface) platform. The simulation domain was decomposed into slabs in the flow direction (x axis), one for each CPU. The number of CPUs varied based on the drop diameter starting from 14 for $\widetilde{d} = 30$ [lu] and up to 20 for $\widetilde{d} = 60$. Depending on the drop diameter the duration of simulations ranged from several hours for the smallest drops to four days for the largest drops.

The details on the choice of the collision operator and related numerical parameters are discussed first. Only two collision operators were considered in the present study: a Bhatnagar-Gross-Krook (BGK)[53] or single-relaxation-time (SRT) and a two-relaxation-time (TRT).[46] The relaxation times (or symmetric contributions if TRT is used) for the f particle distribution function τ_c and τ_d are fixed by the kinematic viscosity of the liquids (36) and will not be changed. The relaxation time for the g distribution function can be tuned to obtain stable, accurate results. Based on test simulations τ_g equal to $1/(3 - \sqrt{3})$ was utilized.[49,54] This value of τ is called the optimum value. Two simulations of a 2.0 mm diameter drop were carried out to outline the impact of the collision operator. Case 1 utilized TRT for both f and g with "magic" numbers $\Lambda_{eo}^f = \Lambda_{eo}^g = 1/12$ and the optimum value of τ_g^s. Case 2 stands for BGK for both f and g and optimum τ_g. It can be noted that when $\tau_g^s = 1/(3 - \sqrt{3})$ and $\Lambda_{eo}^g = 1/12$ the anti-symmetric relaxation time τ_g^a is also equal to $1/(3 - \sqrt{3})$ and TRT for g reduces to BGK. Thus, with this choice of parameters the influence of the collision operator for f is demonstrated.

The evolution of the drop rise velocity for both cases together with terminal drop shape is shown in Fig. 3. The reference value of 2.0 mm drop terminal velocity[14] is 56.92 mm/s. The
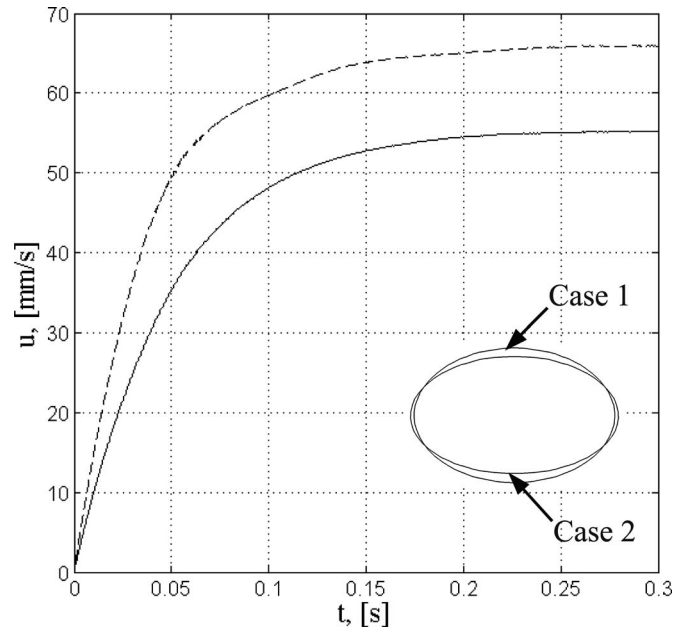
FIG. 3. The evolution of 2 mm drop rise velocity in time and terminal drop shape for different cases. ——Case 1 (TRT); ------case 2 (BGK).

deviation between this reference velocity and velocities obtained in Cases 1 and 2 is 3% and 15.8%, respectively. In addition, slight drop shape oscillations are observed in Case 2. It can be seen from the drop rise velocity time series that does not evolve monotonously. No shape oscillations for a 2.0 mm drop take place during neither experiments nor Case 1. Moreover, the terminal drop shape is different in Cases 1 and 2. The reference aspect ratio (see definition below) is $E = 0.66$, while the values obtained in Cases 1 and 2 are 0.65 and 0.55, respectively. Based on this comparison we will be using a TRT scheme in the remainder of this paper.

The influence of "magic" numbers Λ_{eo} was also examined. If $\Lambda_{eo} = 1/4$ or $1/6$ are specified for both f and g the simulations are unstable. If $\Lambda_{eo}^f = 1/12$ is kept and $\Lambda_{eo}^g = 1/4$ or $1/6$ the simulations are also unstable. Thus, for the n-butanol/water system the simulations are accurate and stable for a wide range of drop diameters only when $\Lambda_{eo}^f = \Lambda_{eo}^g = 1/12$ and $\tau_g^s = 1/(3 - \sqrt{3})$. The analyses of stability and high-order truncated corrections of physically simpler system performed by Ginzburg[55] showed that $\Lambda_{eo} = 1/12$ with the BGK collision operator removes the third-order advection error. Additional investigation of the numerical scheme for the present complex physical system is required to further justify the choice of "magic" numbers. This is beyond the scope of the present paper.

Hence, for the rest of the simulations the following parameters were used: TRT collision operator with $\Lambda_{eo}^f = \Lambda_{eo}^g = 1/12$, $\tau_g^s = 1/(3 - \sqrt{3})$, the mobility coefficient $\Gamma = 8$ and the mobility $M = 2.31$. For this base set of parameters the surface tension related values were $A = -4.3 \times 10^{-3}$, $\kappa = 2.8 \times 10^{-3}$.

The diffuse interface method adopted here is prone to spurious currents over the interface due to discretization of the velocity space. However, the velocities related to spurious currents are several orders of magnitude smaller than the physical velocities. The equilibration of a single stationary drop was simulated with the same stencils and relaxation times as mentioned before. Spurious velocities over the interface were 10^{-4}–10^{-5} in lattice units, while the order of the velocity field in the rising drop simulation is of 10^{-2} in lattice units.

To verify the newly developed computer code and numerical technique, sensitivity analyses have been carried out on simulation domain size and mesh resolution. In addition, the correctness of the moving reference frame implementation has been checked. The results are presented below.
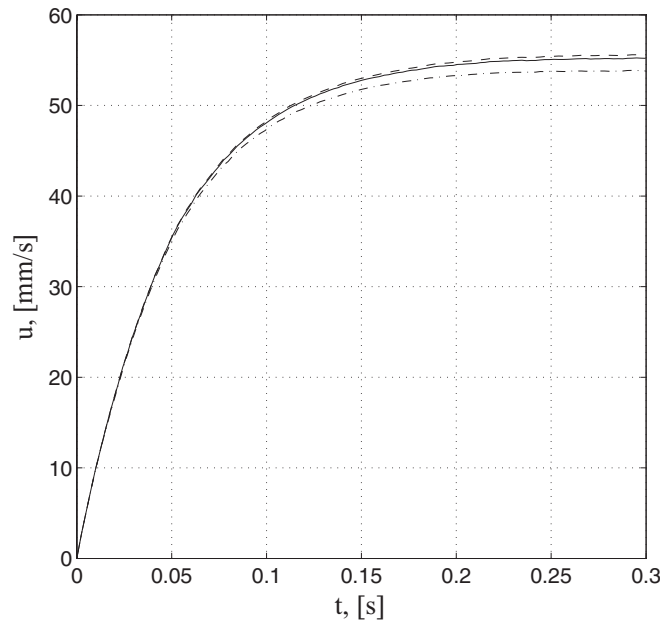
FIG. 4. Domain size influence. The evolution of 2.0 mm drop rise velocity in time for different simulation domain widths. The length of the domain is $14\widetilde{d}$; $-\cdot-\cdot-W = 2\widetilde{d}$; ——$W = 3\widetilde{d}$; ------$W = 4\widetilde{d}$.

A. Domain size influence

The proper simulation domain size should have such width and length that wall confinement effects are negligibly small and there is no impact from the outflow boundary. On the other hand, the size of the domain should be reasonable to avoid extensive computations. The simulations of 2.0 mm drops were carried out in domains with the width W (see Fig. 1) equal to 2–4 drop diameters. All computations were performed in a moving reference frame with drop diameter $\widetilde{d} = 30$ [lu] and length of the domain $L = 14\widetilde{d}$.

The terminal rise velocity was used to assess the wall effects for various domain sizes. The resulting drop terminal velocities for $W = 2\widetilde{d}$, $3\widetilde{d}$, and $4\widetilde{d}$ are 53.81, 55.21, and 55.58 mm/s, respectively. In Fig. 4, the velocity evolution in time is shown. The terminal velocity of the drop obtained in the narrowest domain is within 5% of the one corresponding to the widest domain. The relative deviation of the steady-state velocity obtained for $W = 3\widetilde{d}$ and $W = 4\widetilde{d}$ is less than 1%. Thus, the simulation domain width was chosen to be $W = 3\widetilde{d}$ to limit computational cost. In addition, the width of the domain caused only minor changes of the drop shape in the steady-state regime.

The influence of the simulation domain length was checked again using 2.0 mm drop simulations. The moving reference frame implementation requires the outflow boundary condition. The entire flow is influenced by the outlet boundary location: it is necessary to make sure that the wake behind the drop becomes fully developed and does hardly interfere with the outlet. Several simulation domain lengths L were considered equal to 8, 10, 12, 14, and 16 drop diameters. The terminal drop velocity for the case with $L = 8\widetilde{d}$ is 55.04 mm/s, and for the case $L = 16\widetilde{d}$ the velocity is 55.22 mm/s. Thus, the influence of simulation domain length on terminal drop rise velocity is negligibly small. If not specified otherwise, the simulation domain length was set to $14\widetilde{d}$.

B. Mesh resolution

The accuracy of the results obtained using the basic set of parameters (discussed in Sec. III C) was examined. Two sensitivity analyses on mesh resolution were performed: mesh refinement
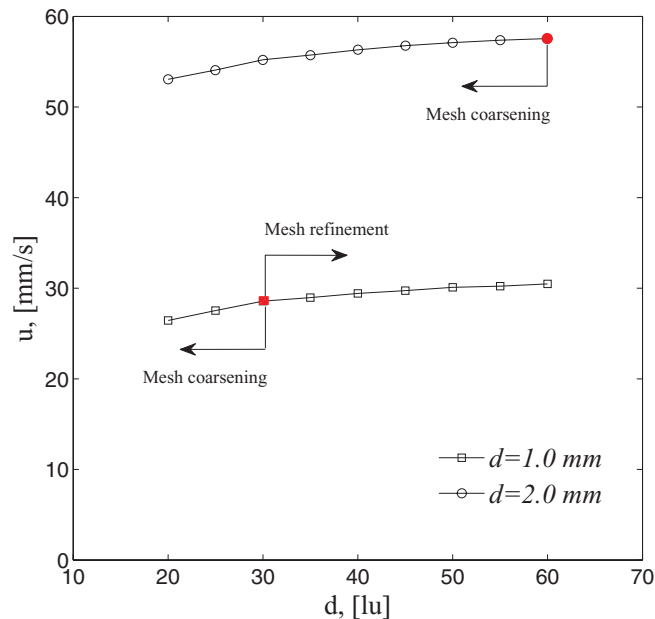
FIG. 5. Mesh resolution. Terminal drop velocity as a function of drop diameter $\widetilde{d}$ in lattice units for 1.0 and 2.0 mm drops obtained.

($f_m > 1.0$) and mesh coarsening ($0.0 < f_m < 1.0$). In both procedures the absolute value of the interface thickness was kept constant ($\xi = 1.14$).

Mesh refinement was performed for simulations of 1.0 mm drops with domain size $12\widetilde{d} \times 3\widetilde{d} \times 3\widetilde{d}$. Six drop diameters in lattice units were considered with corresponding length scaling factors, or mesh steps, in the range $C_d = 1.7 \times 10^{-5} - 2.9 \times 10^{-5}$ m. The resulting terminal drop velocities are plotted in Fig. 5. The terminal drop velocity of the 1.0 mm drop obtained using the basic set of parameters with $\widetilde{d} = 30$ [lu] is depicted by the red square. The relative deviation of the velocity between the basic mesh and the finest mesh is 6.2%. The basic set of parameters is adopted further for the simulations, since it is a good balance between accuracy and simulation time.

Mesh coarsening has also been checked for the 1.0 mm drop. Two cases were simulated with drop diameters 25 and 20 [lu], the corresponding length scaling factors are 4.0×10^{-5} and 5.0×10^{-5} m. The results are shown in Fig. 5: the relative deviation of terminal velocity between 20 and 30 [lu] drops is 7.5%, while the deviation between 20 and 60 [lu] drops is 13.2%.

A mesh coarsening procedure has been applied for a 2.0 mm drop. With the basic set of parameters such drop is represented by a 60 [lu] drop diameters in lattice space (red circle in Fig. 5). Eight smaller drop diameters in lattice space were considered with the mesh step in the range $C_d = 3.33 \times 10^{-5} - 10.0 \times 10^{-5}$ m. The domain size was equal to $14\widetilde{d} \times 3\widetilde{d} \times 3\widetilde{d}$. The terminal drop velocities for all cases are shown in Fig. 5. The relative deviation between the terminal velocity obtained with the basic set of parameters ($\widetilde{d} = 60$ [lu] for 2.0 mm drop) and the rescaled parameters for coarser drops with $\widetilde{d} = 30$ [lu] ($f_c = 0.5$) is 4%. This value of the coarsening factor is used for all drops larger than 2.0 mm, since it reduces the domain size and, subsequently, the simulation time while giving result that are in good agreement with those obtained using a finer mesh.

C. Moving reference frame implementation

In the present study the numerical simulations of a *n*-butanol drop moving in water were performed in a moving reference frame. Since the moving frame implementation involves modification of the governing equations it is important to verify the results by confronting them to those obtained on a stationary reference frame.
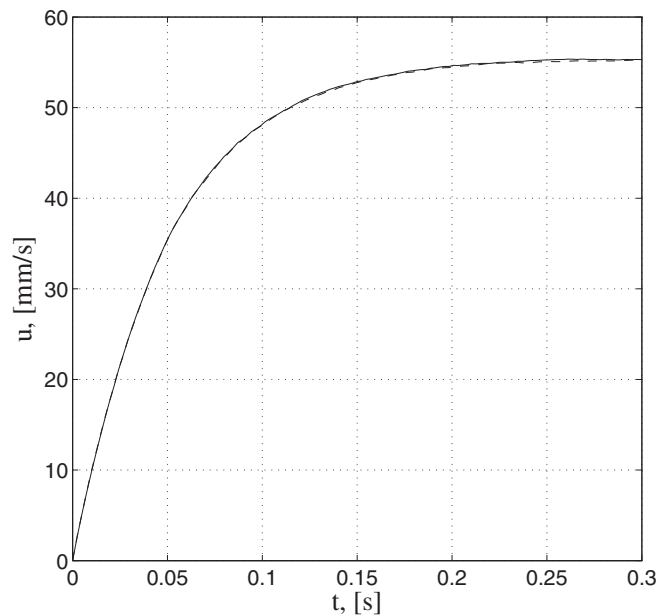
FIG. 6. Time evolution of terminal rise velocity of 2.0 mm drop calculated in two test cases: ——stationary reference frame; ------moving reference frame.

A 2.0 mm drop was simulated both in stationary and moving reference frames. The diameter of the drop in lattice space was $\widetilde{d} = 30$. The size of the stationary domain was $24\widetilde{d} \times 3\widetilde{d} \times 3\widetilde{d}$. Bounce-back (walls) boundary conditions were imposed on boundaries of the domain with $x = 0$ and $x = L$, specular reflection conditions were applied on all side walls since only a quarter of the domain was considered (see Fig. 1). The initial position of the drop in case of the stationary domain was at a distance $7.5\widetilde{d}$ from the boundary $x = 0$.

In the moving reference frame implementation when a velocity inflow boundary condition is used together with outflow boundary condition, at the beginning of the simulation a pressure wave appears: it moves back and forth over the domain and eventually dissipates.[50] The cause of the wave is the inconsistency of the initialization: the density (pressure) field does not match the velocity values set at the inflow boundary.[56] Since the simulated drop is initially at rest and smoothly accelerates by the external gravity force, the imposed velocity at the inlet boundary u_{in} is zero at the first time step and increases slowly over the time. Thus, the impact of the pressure wave on the flow development during the initial time steps is small as will be shown below.

The development of the drop rise velocity in time for both test cases carried out using stationary and moving reference frames is presented in Fig. 6. The results are in excellent agreement. The drop terminal velocity obtained using the moving reference frame is 55.21 mm/s and 55.35 mm/s using the stationary frame of reference. The streamlines corresponding to both frames have also been compared. To enable this comparison between the moving and stationary frames, the velocity of the moving frame was subtracted from the velocity field computed on stationary frame. The streamlines together with the x-component of the velocity field for the test simulations at time instants 0.05, 0.15, and 0.3 s are shown in Fig. 7. The last moment is during steady-state. The white curve represents the interface. The external flow is from the right to left, the front of the drop is facing the positive x-direction. As one can see, the results agree well. The streamlines at time step 0.05 s are identical, which means there is no impact of the inflow/outflow boundary conditions or inconsistency of the initialization in the moving frame implementation. The slight difference of streamline behavior in the wake of the drop is attributed to the sensitivity of streamlines plotting: there is a significant influence of the exact value of the subtracted velocity of the moving frame on the streamline pattern. Since the magnitude of the velocities in that regions is small compared to the velocity of the drop, even slight differences of velocity cause notable changes in streamlines behavior. Since the deviation
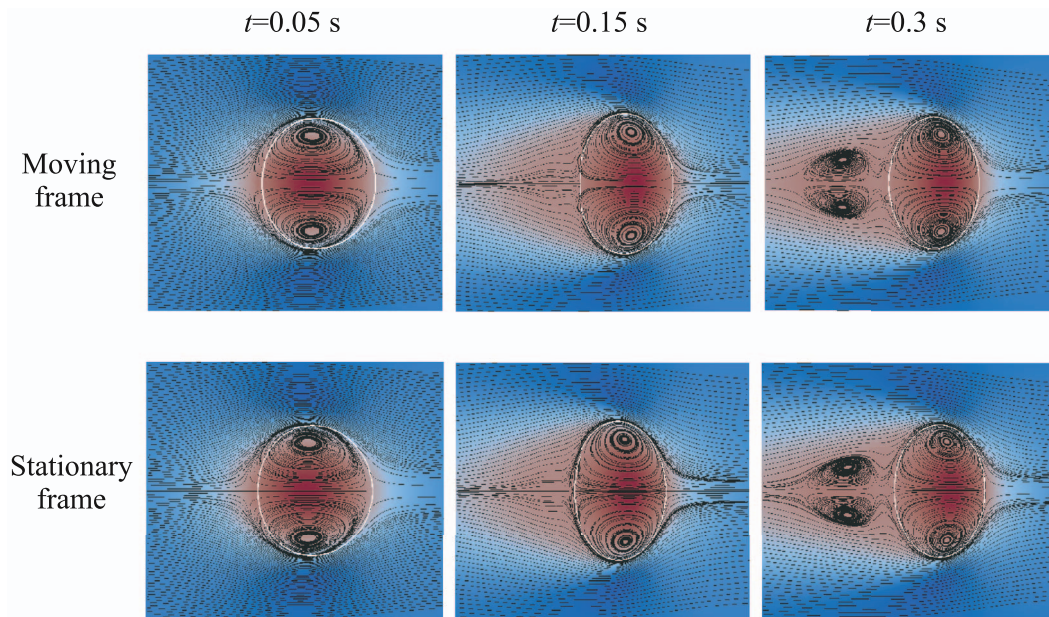
FIG. 7. Streamlines with x-component of velocity for 2.0 mm drop in two cases: moving reference frame and stationary reference frame. The white curve represents the interface.

of terminal velocities in both cases is negligible, the moving reference frame approach was adopted for the rest of the simulations.

V. ANALYSES OF *N*-BUTANOL DROP MOTION IN WATER

The numerical simulations of n-butanol droplets motion in water have been performed for drops within the diameter range 1.0–4.0 mm with the aim to observe three flow regimes relevant to extraction processes: spherical, deformed, and oscillating drops. For each drop the terminal rise velocity and drop deformation were analyzed. The terminal velocity of non-oscillating droplets was determined when steady-state had been reached after an acceleration period. The mean terminal velocity for shape oscillating drops was evaluated by averaging the rise velocity over the time spent on several shape oscillations. Each simulation was run until the steady-state was reached for non-oscillating drops or when the velocity of oscillating drops reached the steady oscillations. The terminal velocity values obtained in this study were compared to experimental and numerical results reported by Bertakis *et al.*,[4] a semi-empirical correlation proposed by Henschke (see Ref. [4] for details) and numerical results obtained by Bäumler *et al.*[14] The maximum diameter of the drop considered by Bäumler *et al.*[14] was 3.1 mm, Bertakis *et al.*[4] considered the maximum drop diameter of 3.48 mm in experiments and 4.0 mm in simulations.

The terminal velocities as a function of drop diameter are plotted in Fig. 8. The results are in good agreement for drops up to 3.0 mm in diameter. The relative deviation of velocity for the 3.0 mm drop compared to simulation results of Bertakis *et al.*[4] is 8% and compared to Bäumler *et al.*[14] is 2%. The relative deviation in the terminal velocity for the 4.0 mm drop calculated here with the result presented by Bertakis *et al.*[4] is 20% which is the largest deviation between the results of the present study and the existing data. However, several facts should be taken into account when comparing the results. As is shown later, Bertakis *et al.*[4] performed simulations over a time window that is not long enough for the drop rise velocity to reach steady-state, and the values of the velocity might be larger than outlined. In addition, the authors mentioned that the larger the velocity of the drop, the bigger the relative error of the terminal velocity measurements (up to 2.1% for the fastest one). Bäumler *et al.*[14] obtained the maximum velocity of the drop at maximum considered drop diameter. A more detailed discussion of the results is presented below.
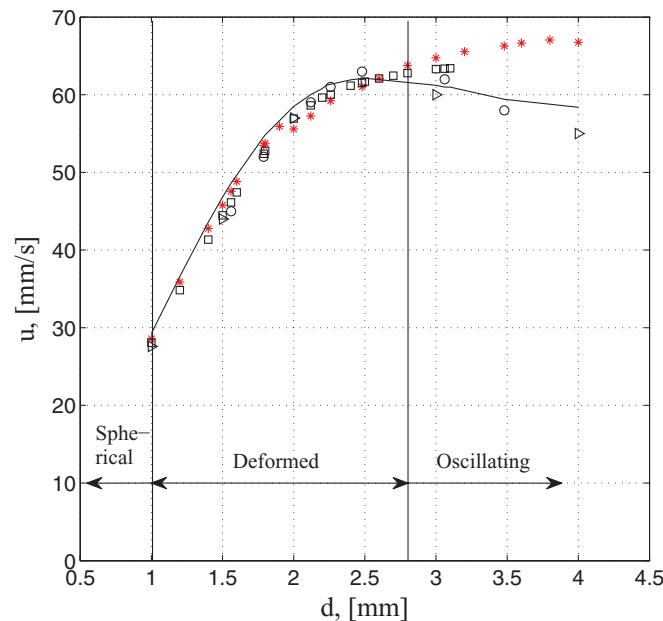
FIG. 8. Simulated drop terminal velocities (*) of *n*-butanol drops in water as a function of drop diameter compared to semi-empirical correlation proposed by Henschke (solid line), experiments (○), and simulations (▷) by Bertakis *et al.*,[4] simulations (□) by Bäumler *et al.*[14]

In the experimental data by Bertakis *et al.*[4] the maximum velocity is reached at $d = 2.48$ mm, according to the data fit (Henschke model) the maximum velocity is found at 2.5 mm, whereas the simulations of Bertakis *et al.*[4] have the maximum at 3.0 mm; just slightly below the simulations of Bäumler *et al.*,[14] with 3.1 mm. In present simulation the maximum velocity is reached for the droplet of 3.8 mm diameter. However, it is difficult to clearly distinguish this maximum velocity since the drops with diameter $d \geq 3.5$ mm have close terminal drop velocity values (see Fig. 8).

To describe the shape deformation quantitatively, the aspect ratio E is used, which is defined as the ratio of the two principal axes of the drop.[57] Referring to the simulation domain depicted in Fig. 1, the aspect ratio can be calculated as $E = L_{||}/(2L_{\perp})$, where $L_{||}$ is the size of the drop parallel to the flow direction and $L_{\perp}$ is the size of the drop perpendicular to the flow direction. $E = 1$ means that the droplet has spherical shape.[57] If $E < 1$ the shape of the drop is called "oblate" and if $E > 1$, then it is a "prolate" shape. In all simulations presented here only spherical and oblate drop shapes were observed at steady-state drop motion. The value of E was compared to the results of Bäumler *et al.*[14] who fitted their simulated data with the following equation:

$$E = e^{-a\,\mathrm{Eo}^{b}}, \tag{44}$$

where $a = 0.081$ and $b = 1.299$. The simulated aspect ratio as a function of Eötvös number Eo is plotted in Fig. 9 together with the results obtained by Bäumler *et al.*[14] Good agreement is observed.

According to Michaelides[57] if $E \geq 0.95$ the drop can be regarded as spherical. Among the drop diameters considered in the present simulations only the 1.0 mm drop has a spherical shape at steady-state. Drops with larger diameters are either deformed or shape-oscillating. Small drops accelerate monotonously over the time and, finally attain a steady-state terminal velocity. In Fig. 10(a), one can see the evolution of the drop rise velocity in time for 1.0, 1.5, and 2.48 mm drops. The acceleration period for 1.0 mm drop is less than 0.2 s which is in good correlation with results of Bertakis *et al.*[4] and Bäumler *et al.*[14] For all drops with diameter $d > 2.0$ mm vortices appear in the wake.

When drop diameters exceed 2.6 mm a different behavior of the drop is noticed: slight oscillations appear over the acceleration period. The possible reason behind this is the low interfacial tension of the *n*-butanol/water system compared, for example, to a toluene/water system. In
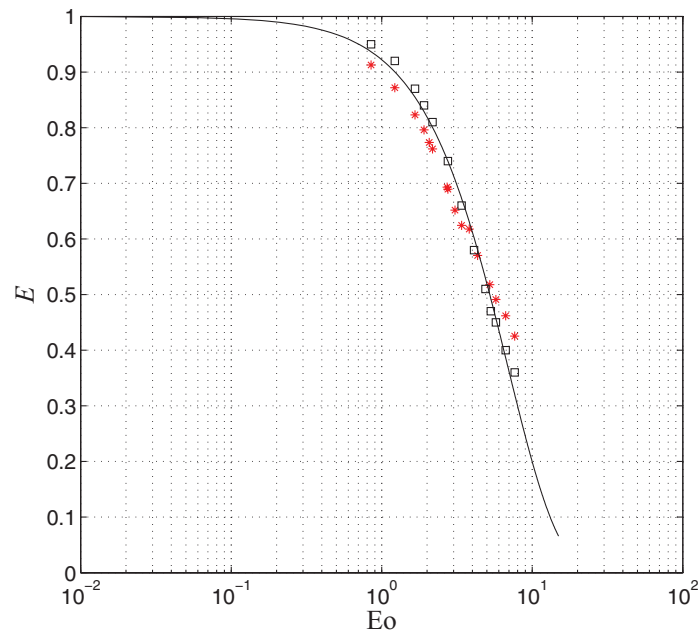
FIG. 9. Simulated aspect ratio E (*) as a function of Eötvös number Eo in comparison with Bäumler et al.[14] (the results of numerical simulation due to Ref. 14 are denoted as □; the solid curve stands for the data fitting curve described by Eq. (44)).

Fig. 10(b), time series of the rise velocity for drops with diameter 2.6 and 2.8 mm are depicted. The amplitude of oscillations of 2.6 mm drop is so small that they are damped during the acceleration period, and the drop reaches a steady terminal velocity. The acceleration of the 2.8 mm drop goes along with more developed oscillations that do not vanish over the time. This denotes the onset of shape oscillations of drops with diameter $d \geq 2.8$ mm. The terminal velocity of the drop oscillates around the mean value at the steady-state regime. According to Bertakis et al.[4] the onset of oscillations is at approximately 2.86 mm which agrees well with the present results.

The rise velocity of 3.0 mm drop is presented in Fig. 10(c). The behavior is in excellent agreement with Bäumler et al.[14] (see their Fig. 12). The following terminal velocities of the drop are obtained in present simulation, numerical simulation by Bertakis et al.[4] and Bäumler et al.,[14] respectively: 64.75, 60.0, and 63.30 mm/s. Even though all results are in good agreement, the lower value obtained by Bertakis et al.[4] could be explained by the fact that simulations were carried out only until 0.4 s after startup, while the velocity of the drop keeps increasing until $t = 0.8$ s.

The larger the drop diameter, the longer the acceleration period. The amplitude of the velocity oscillations also becomes larger, both in accelerating and steady regimes. A representative result of the rise velocity evolution in time in the oscillating drop regime is shown in Fig. 10(d) that relates to a 3.48 mm drop. A further increase in drop diameter leads to significant drop deformations at initial times that changes the value and oscillations behavior of drop rise velocity. The results of the 3.8 mm drop terminal velocity calculations are shown in Fig. 10(e). For all previous oscillating drops (Figs. 10(c) and 10(d)), the second peak during the acceleration period was higher than the first one. In contrast, for the 3.8 mm drop, the value of the second peak is below the value of the first one. The evolution of rise velocity for later times has the same trends as discussed earlier. To see the difference in drop deformations at initial times, the flow streamlines together with the drop shape are presented in Fig. 11 for the 3.48 and 3.8 mm drops. At $t = 0.1$ s, the shape of the drops and flow streamlines are similar in both cases. However, at $t = 0.2$ s, the 3.8 mm drop deforms in a way (possibly because of the low surface tension and high velocity compared to the velocity of the 3.48 mm drop at this time instant) that at later time $t = 0.4$ s the droplet gets a concave shape. In addition, the size and shape of the wake behind the drops is different. The concave shaped drop has a wider and shorter wake compared to the ellipsoidal drop.
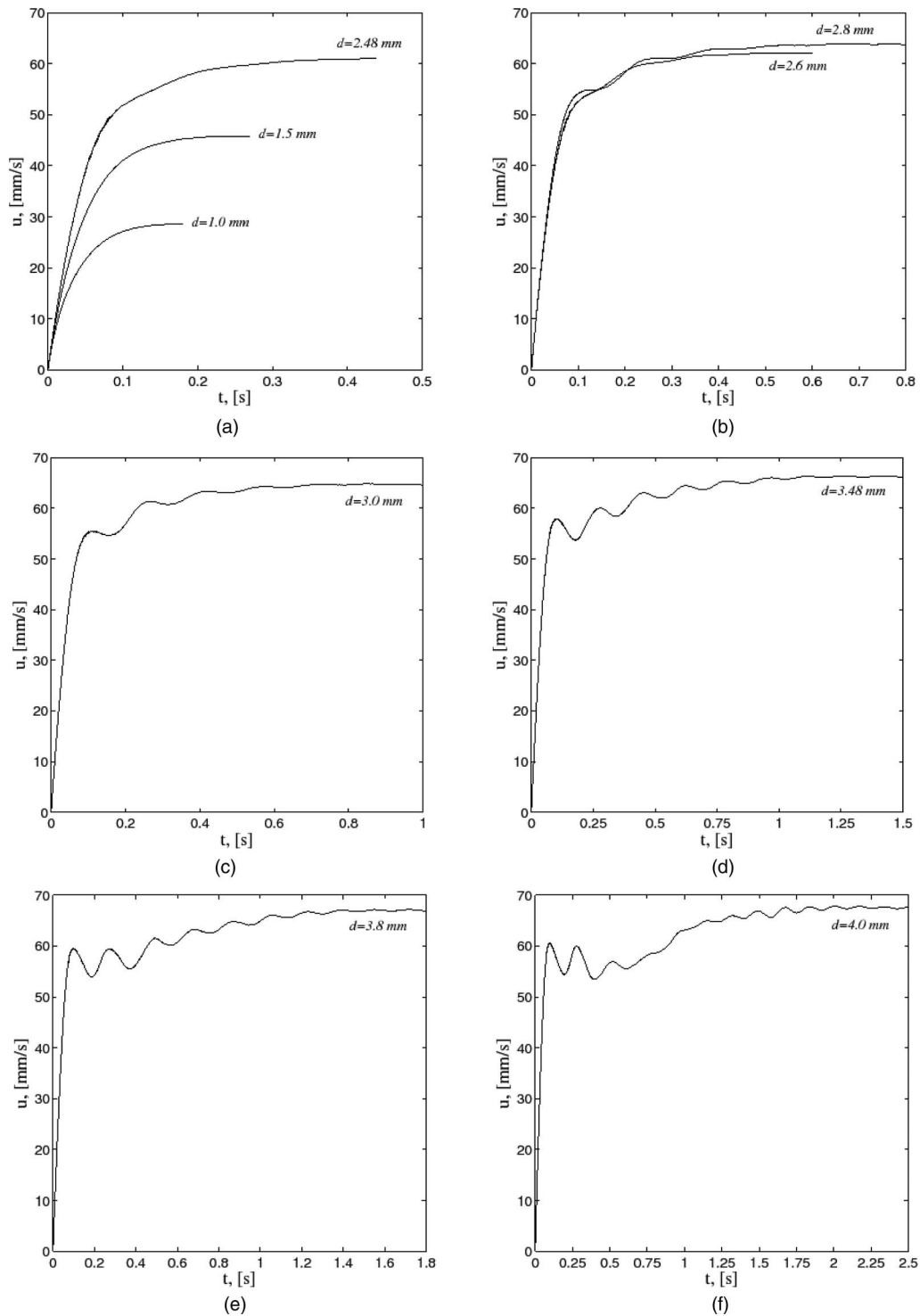
FIG. 10. Drop rise velocity as a function of time for different drop diameters; (a) 1.0 mm drop in spherical regime and 1.5, 2.48 mm drops in deformed regime; (b) 2.6 and 2.8 mm drops refer to transition between deformed and oscillating droplets; (c) 3.0 mm drop; (d) 3.48 mm drop; (e) 3.8 mm drop; (f) 4.0 mm drop is the largest simulated drop in the present study.
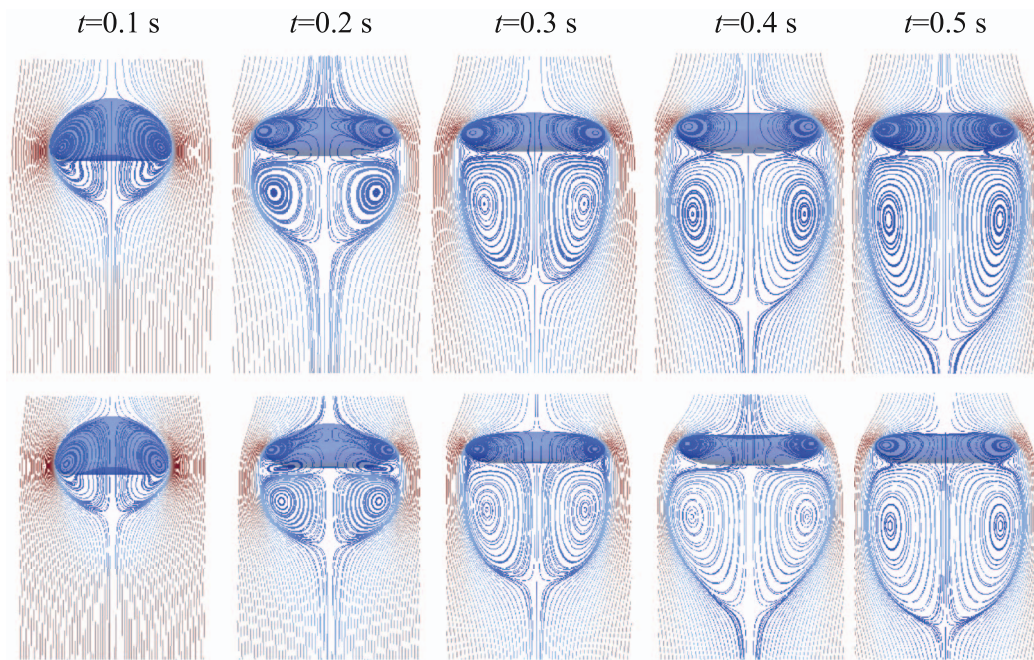
FIG. 11. Streamlines and drop shape for $d = 3.48$ mm (upper row) and $d = 3.8$ mm (bottom row) drops at different moments.

Notable differences in the drop rise velocity evolution are observed for the 4.0 mm drop (Fig. 10(f)). After significant velocity oscillations and shape deformations at initial time steps, the velocity rapidly increases and, finally, the droplet attains a steady regime with oscillations around a mean value. The 4.0 mm drop deformation at different times are presented in Fig. 12. After significant deformation up to $t = 0.6$ s the droplet gets a concave shape and with slight oscillations accelerates while changing its shape to ellipsoidal with a flattened surface on top. Finally, the drop oscillates around the mean terminal velocity and ellipsoidal drop shape. The mean terminal drop velocity is equal to 66.75 mm/s, while Bertakis et al.[4] obtained a value of 55.0 mm/s. It should be mentioned that the simulations of the 4.0 mm drop were carried out by Bertakis et al.[4] only until $t = 0.7$ s. As can be seen in Fig. 10(f) the velocity keeps increasing until 1.75 s. The drop velocity value at $t = 0.7$ s obtained in the present study is 56.25 mm/s which is close to Bertakis et al.[4] Also the evolution of the rise velocity in time agrees well with reference data.

To validate our numerical results of shape deformation the well known diagram by Clift et al.[37] is used. The simulated data are plotted in the graphical correlation in Fig. 13. The plot shows the Reynolds number versus Eötvös for the Morton number of n-butanol/water system equal to 1.23 $\times 10^{-6}$. The simulated data excellently match the correlation: the 1.0 mm drop lies exactly on the curve dividing the regions of spherical and ellipsoidal drops. The correlation appears to better predict the behavior of n-butanol water system for larger drop diameters.

In addition, the numerical data were organized using Reynolds and Weber numbers. In contrast to the previous correlation, the We number contains the terminal drop velocity, and shows the ratio of continuous phase internal fluid stresses (that cause the deformation of the drop) and surface tension stresses resisting the deformation. The plot is shown in Fig. 14, where the steady state shape of the drops are also depicted (for the shape oscillating drops the shape at the mean terminal velocity is presented). For We ≤ 1.0, only negligibly small deviation of the drop shape from a sphere is observed. With the increase of We number, the drop is more deformed.

The ratio between Weber and Reynolds numbers gives a capillary number Ca $= u\mu_c/\sigma$. The capillary number measures the balance between two competing effects: the viscous stress of the continuous liquid that causes the drop deformation, and capillary stress that resists the deformation. In Fig. 15, the simulated capillary number is plotted as a function of Eötvös number. With the increase of Eo (i.e., the drop diameter since Eo $\sim d^2$) the Ca number approaches a constant value.
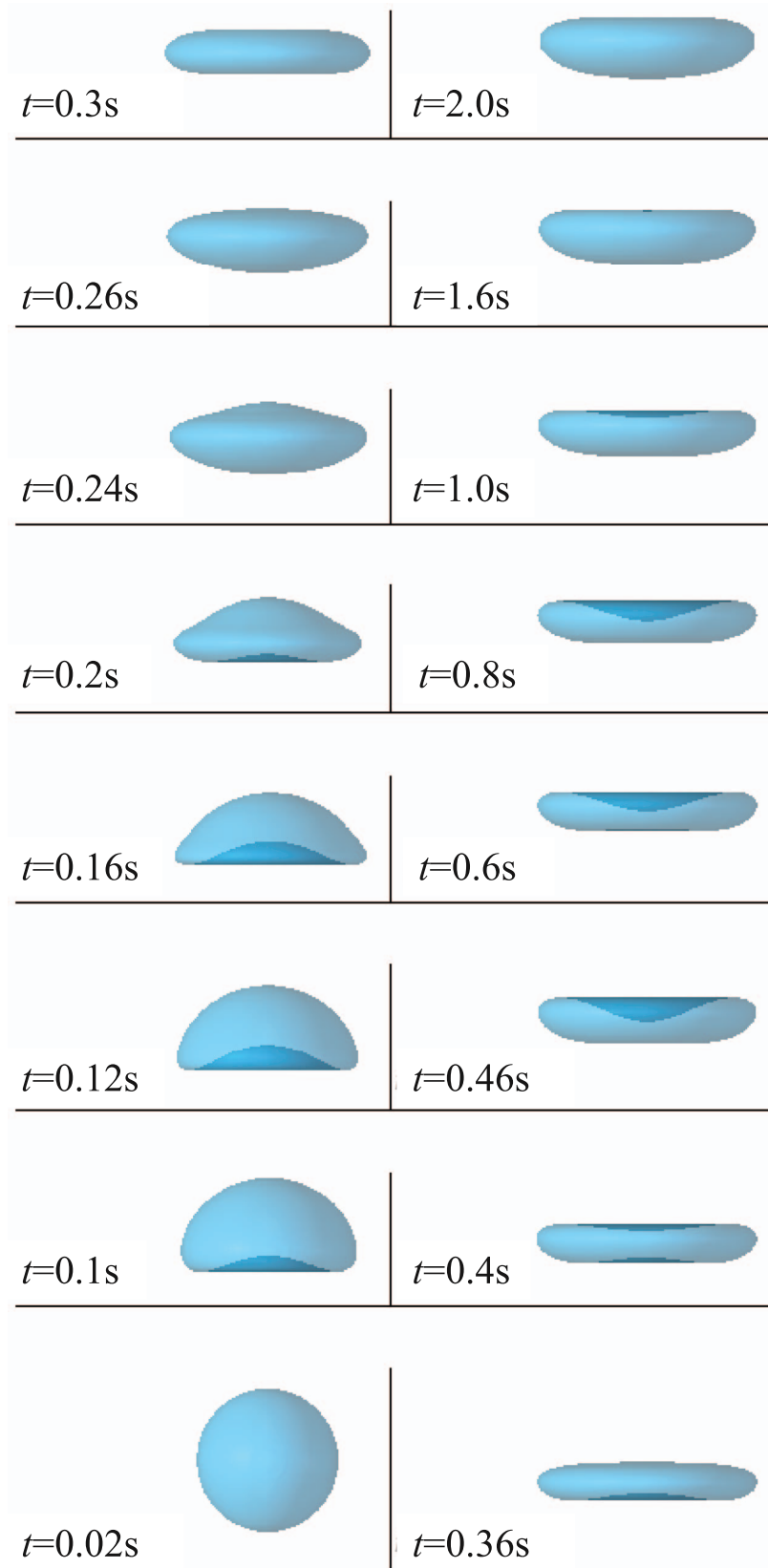
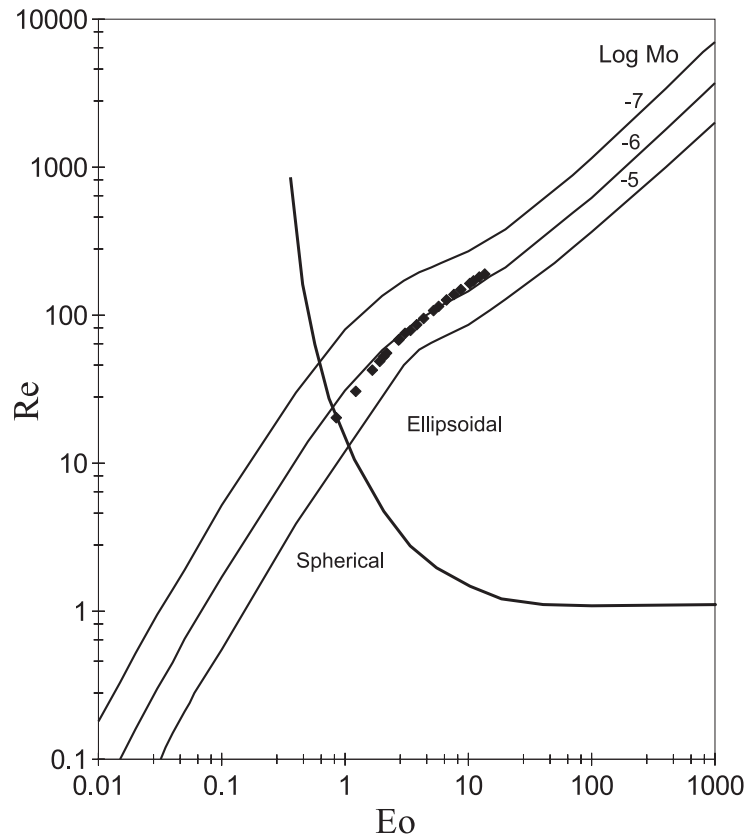FIG. 12. The *n*-butanol drop deformation of 4.0 mm diameter at different time steps.

FIG. 13. Comparison of simulated Reynolds numbers Re as a function of Eötvös number Eo for Morton number Mo $= 1.23 \times 10^{-6}$ to the graphical correlation by Clift *et al.*[37]
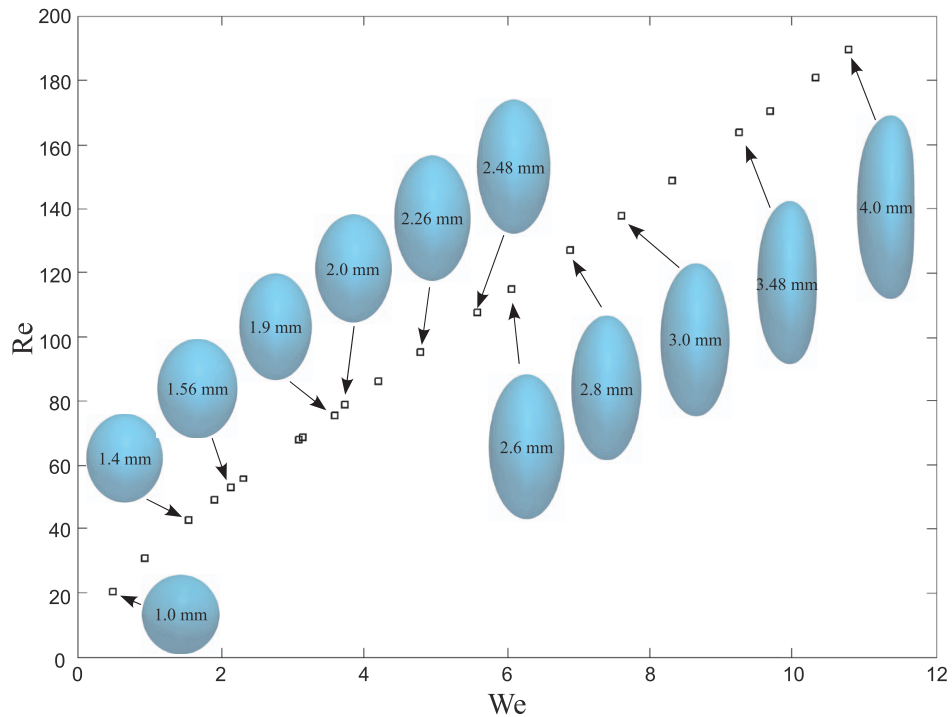

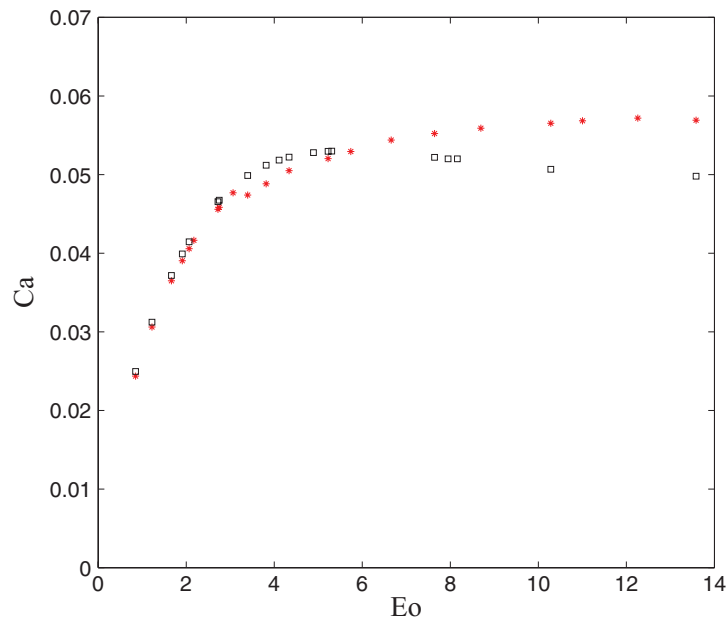FIG. 14. Simulated Reynolds number Re versus Weber number We plotted with drop shapes in steady-state.

FIG. 15.   Capillary number Ca versus Eötvös number Eo; (*) present simulations; (□) the Ca number value plotted using the terminal velocity obtained with semi-empirical correlation proposed by Henschke.[14]

The drop enters the shape oscillation regime when Eo $\geqslant$ 7.0. As one can see from the graph this is the point where Ca gets to a constant value of 0.056. During the shape oscillations viscous and internal forces balance not letting the drop break or return to a stable shape. With further increase of drop diameter the surrounding liquid might cause more significant drop deformations and break the drop.

VI. CONCLUSION

In this paper numerical simulations of single n-butanol drops rising in water under the influence of gravity are presented. The free energy LBE model with TRT collision operator was used to perform three-dimensional simulations of this binary system in order to determine the drop terminal velocity and its shape. The drop diameters that were studied 1.0–4.0 mm spanned the regions of spherical, deformed, and oscillating droplets, allowing to test the numerical technique under different conditions relevant to liquid-liquid extraction processes. The simulations were carried out in a moving reference frame to reduce the domain size, and thus the computational cost. The computer code was developed in FORTRAN 90 with MPI for parallel processing.

The proposed scaling procedure allowed to determine the parameters in lattice space, where the LBE models operate, that correspond to the real physical parameters of the given binary system. It was outlined that in order to determine the proper values of the LBE parameters it is necessary to validate the results with a benchmark solution. In our case the benchmark data were the experimental results and the results of simulations obtained using different numerical techniques. Once the numerical approach is validated, it can be applied for simulations of multiphase systems in other problem statements, e.g., consideration of n-butanol drop breakup or coalescence in water, or multiple drops interaction in laminar shear of fully developed turbulent flow.

The simulation parameters as computational domain size, mesh resolution, and LBE numerical parameters were tested to verify the developed computer code. For negligible effects of boundary walls, the width of the domain should be at least three drop diameters.

The mesh resolution has a significant effect on the results. It is important to capture the essential drop deformations and oscillations, circulations inside the drop and wake development behind the drop. Mesh refinement has been performed to determine the required mesh resolution: the relative

deviation between the terminal velocity obtained on the coarsest and the finest grids is 13.2% for a 1.0 mm drop. For the same drop, the relative deviation in drop velocity obtained on the mesh resolution with which most of the simulations have been carried out and the finest mesh is 6.2%.

The simulations captured drop acceleration, shape deformation, steady motion with constant velocity of non-oscillating drop, and shape-oscillating motion of drops in the oscillatory regime. The results obtained in the study have been compared to experimental data and numerical simulations using other methods. The results show that the numerical technique can be adopted to perform multiphase simulations with moving and deforming interfaces. The results of the simulations are in good agreement with experimental and numerical data. The deviation in terminal drop velocity for small drop diameters is within 5% and up to 20% for the largest one. The capability of the method to capture the drop shape deformation especially in the oscillating regime is also demonstrated. The results are in excellent correlation with the standard reference diagram by Clift *et al.*[37] for predicting the shape of fluid particles. In addition, it was outlined that the regime of shape oscillations of the drop in the considered drop diameter range is characterized by an almost constant capillary number of Ca = 0.056.

The regimes of drop motion did not cover drop breakup. As future work, the *n*-butanol drops in water under simple shear flow will be considered. Such a problem will allow us to test the capability of the developed numerical technique of interface disintegration capturing. Also drop coalescence will be considered. This is one of the most challenging problems to solve since the drawback of the utilized interface capturing technique is artificial merging of the drops even in the cases where the drops should not coalescence. After the developed numerical tools have been tested using these benchmark problems, *n*-butanol drop dispersions in water will be considered with hundreds of dispersed drops subjected to turbulent flow conditions.

APPENDIX: THE D3Q19 MODEL PARAMETERS

The D3Q19 model is used to discretize the velocity space.[58] The lattice vectors are separated into two groups. Velocities c_{1-6} point in the nearest neighbor directions

$$\begin{pmatrix} c_{x1-6} \\ c_{y1-6} \\ c_{z1-6} \end{pmatrix} = \begin{bmatrix} c & -c & 0 & 0 & 0 & 0 \\ 0 & 0 & c & -c & 0 & 0 \\ 0 & 0 & 0 & 0 & c & -c \end{bmatrix}$$

and c_{7-18} point in the 12 square diagonal directions

$$\begin{pmatrix} c_{x7-18} \\ c_{y7-18} \\ c_{z7-18} \end{pmatrix} = \begin{bmatrix} c & -c & c & -c & 0 & 0 & 0 & 0 & c & -c & c & -c \\ c & c & -c & -c & c & -c & c & -c & 0 & 0 & 0 & 0 \\ 0 & 0 & 0 & 0 & c & c & -c & -c & c & c & -c & -c \end{bmatrix}. \qquad (A1)$$

The equilibrium distributions[47] f_q^{eq}, g_q^{eq} for population $q = (1–18)$ are calculated as follows:

$$f_q^{\mathrm{eq}} = \frac{w_q}{c^2}\left(p_0 - \kappa(\partial_{xx}^2\phi + \partial_{yy}^2\phi + \partial_{zz}^2\phi) + e_{\alpha q}\rho u_\alpha + \frac{3}{2c^2}\left[e_{\alpha q}e_{\beta q} - \frac{c^2}{3}\delta_{\alpha\beta} \right]\rho u_\alpha u_\beta \right) +$$

$$\frac{\kappa}{c^2}\left(w_q^{xx}\partial_x\phi\partial_x\phi + w_q^{yy}\partial_y\phi\partial_y\phi + w_q^{zz}\partial_z\phi\partial_z\phi + w_q^{xy}\partial_x\phi\partial_y\phi + w_q^{xz}\partial_x\phi\partial_z\phi + w_q^{yz}\partial_y\phi\partial_z\phi \right), \qquad (A2)$$

$$g_q^{\mathrm{eq}} = \frac{w_q}{c^2}\left(\Gamma\mu + e_{\alpha q}\rho u_\alpha + \frac{3}{2c^2}\left[e_{\alpha q}e_{\beta q} - \frac{c^2}{3}\delta_{\alpha\beta} \right]\phi u_\alpha u_\beta \right), \qquad (A3)$$

while the distributions for $q = 0$ are given by

$$f_0^{\text{eq}} = \rho - \sum_{q=1}^{18} f_q^{\text{eq}}$$

$$g_0^{\text{eq}} = \phi - \sum_{q=1}^{18} g_q^{\text{eq}}$$

(A4)

and the bulk pressure is $p_0 = c_s^2 \rho + \dfrac{A}{2}\phi^2 + \dfrac{3B}{4}\phi^4$.

And the weights[47] read

$$w_{1-6} = \frac{1}{6}, \quad w_{7-18} = \frac{1}{12},$$

$$w_{1-2}^{xx} = w_{3-4}^{yy} = w_{5-6}^{zz} = \frac{5}{12}, \quad w_{3-6}^{xx} = w_{1-2,5-6}^{yy} = w_{1-4}^{zz} = -\frac{1}{3},$$

$$w_{7-10}^{xx} = w_{15-18}^{xx} = w_{7-14}^{yy} = w_{11-18}^{zz} = -\frac{1}{24},$$

$$w_{11-14}^{xx} = w_{15-18}^{yy} = w_{7-10}^{zz} = \frac{1}{12},$$

$$w_{1-6}^{xy} = w_{1-6}^{yz} = w_{1-6}^{zx} = 0, \quad w_{7,10}^{xy} = w_{11,14}^{yz} = w_{15,18}^{zx} = \frac{1}{4},$$

$$w_{8,9}^{xy} = w_{12,13}^{yz} = w_{16,17}^{zx} = -\frac{1}{4}, \quad w_{11-18}^{xy} = w_{7-10}^{yz} = w_{7-14}^{zx} = 0.$$

(A5)

The stencils for the gradients and Laplacian calculations in the pressure tensor and chemical potential are

$$\partial_x = \frac{1}{12\Delta x}\left[\begin{pmatrix} 0 & 0 & 0 \\ -1 & 0 & 1 \\ 0 & 0 & 0 \end{pmatrix}, \begin{pmatrix} -1 & 0 & 1 \\ -2 & 0 & 2 \\ -1 & 0 & 1 \end{pmatrix} \begin{pmatrix} 0 & 0 & 0 \\ -1 & 0 & 1 \\ 0 & 0 & 0 \end{pmatrix}\right], \qquad (A6)$$

$$\nabla^2 = \frac{1}{6\Delta x^2}\left[\begin{pmatrix} 0 & 1 & 0 \\ 1 & 2 & 1 \\ 0 & 1 & 0 \end{pmatrix}, \begin{pmatrix} 1 & 2 & 1 \\ 2 & -24 & 2 \\ 1 & 2 & 1 \end{pmatrix} \begin{pmatrix} 0 & 1 & 0 \\ 1 & 2 & 1 \\ 0 & 1 & 0 \end{pmatrix}\right], \qquad (A7)$$

where the left, middle, and right matrices show slices of the stencil when $c_{zq} = c$, 0, and $-c$, respectively.

[1] R. E. Treyba, *Liquid Extraction* (McGraw-Hill, New York, 1951).

[2] M. Henschke and A. Pfennig, "Mass-transfer enhancement in single-drop extraction experiments," AIChE J. **45**, 2079 (1999).

[3] M. Wegener, M. Kraume, and A. R. Paschedag, "Terminal and transient drop rise velocity of single toluene droplets in water," AIChE J. **56**, 2 (2010).

[4] E. Bertakis, S. Groβ, J. Grande, O. Fortmeier, A. Reusken, and A. Pfennig, "Validated simulation of droplet sedimentation with finite-element and level-set methods," Chem. Eng. Sci. **65**, 2037 (2010).

[5] S. Hu and R. C. Kintner, "The fall of single liquid drops through water," AIChE J. **1**, 42 (1955).

[6] A. J. Klee and R. E. Treybal, "Rate of rise or fall of liquid drops," AIChE J. **2**, 444 (1956).

[7] P. M. Krishna, D. Venkateswarlu, and G. S. R. Narasimhamurty, "Fall of liquid drops in water: Drag coefficients, peak velocities, and maximum drop sizes," J. Chem. Eng. Data **4**, 340 (1959).

[8] P. M. Krishna, D. Venkateswarlu, and G. S. R. Narasimhamurty, "Fall of liquid drops in water: Terminal velocities," J. Chem. Eng. Data **4**, 336 (1959).

[9] A. I. Johnson and A. E. Hamielec, "Mass transfer inside drops," AIChE J. **6**, 145 (1960).

[10] G. Thorsen, R. M. Stordalen, and S. G. Terjesen, "On the terminal velocity of circulating and oscillating liquid drops," Chem. Eng. Sci. **23**, 413 (1968).

[11] J. R. Strom and R. C. Kintner, "Wall effect for the fall of single drops," AIChE J. **4**, 153 (1958).

[12] R. M. Griffith, "The effect of surfactants on the terminal velocity of drops and bubbles," Chem. Eng. Sci. **17**, 1057 (1962).

[13] A. M. Dehkordi, S. Ghasemian, D. Bastani, and N. Ahmadpour, "Model for excess mass–transfer resistance of contaminated liquid–liquid systems," Ind. Eng. Chem. Res. **46**, 1563 (2007).

[14] K. Bäumler, M. Wegener, A. R. Paschedag, and E. Bänsch, "Drop rise velocities and fluid dynamics behavior in standard test systems for liquid/liquid extraction: Experimental and numerical investigations," Chem. Eng. Sci. **66**, 426 (2011).

[15] J. Petera and L. R. Weatherley, "Modelling of mass transfer from falling droplets," Chem. Eng. Sci. **56**, 4929 (2001).

[16] T. Watanabe and K. Ebihara, "Numerical simulation of coalescence and breakup of rising droplets," Comput. Fluids **32**, 823 (2003).

[17] J. R. Grace, T. Wairegi, and T. H. Nguyen, "Shapes and velocities of single drops and bubbles moving freely through immiscible liquids," Trans. Inst. Chem. Eng. **54**, 167 (1976).

[18] M. Wegener, T. Eppinger, K. Bäumler, M. Kraume, A. R. Paschedag, and E. Bänsch, "Transient rise velocity and mass transfer of a single drop with interfacial instabilities: Numerical investigations," Chem. Eng. Sci. **64**, 4835 (2009).

[19] M. Ohta, S. Yamaguchi, Y. Yoshida, and M. Sussman, "The sensitivity of drop motion due to the density and viscosity ratio," Phys. Fluids **22**, 072102 (2010).

[20] S. Osher and J. A. Sethian, "Fronts propagating with curvature dependent speed: Algorithms based on Hamilton-Jacobi formulations," J. Comput. Phys. **79**, 12 (1988).

[21] M. Sussman, P. Smereka, and S. Osher, "A level set approach for computing solutions to incompressible two-phase flow," J. Comput. Phys. **114**, 146 (1994).

[22] C. W. Hirt and B. D. Nichols, "Volume of fluid (VOF) method for the dynamics of free boundaries," J. Comput. Phys. **39**, 201 (1981).

[23] Y. Y. Renardy, M. Renardy, and V. Cristini, "A new volume-of-fluid formulation for surfactants and simulations of drop deformation under shear at a low viscosity ratio," Eur. J. Mech. B/Fluids **21**, 49 (2002).

[24] D. Jacqmin, "Calculation of two-phase Navier–Stokes flows using phase-field modeling," J. Comput. Phys. **155**, 96 (1999).

[25] V. E. Badalassi, H. D. Ceniceros, and S. Banerjee, "Computation of multiphase systems with phase field models," J. Comput. Phys. **190**, 371 (2003).

[26] A. K. Gunstensen, D. H. Rothman, S. Zaleski, and G. Zanetti, "Lattice Boltzmann model for immiscible fluids," Phys. Rev. A **43**, 4320 (1991).

[27] X. Shan and H. Chen, "Lattice Boltzmann model for simulating flows with multiple phases and components," Phys. Rev. E **47**, 1815 (1993).

[28] T. J. Spencer, I. Halliday, and C. M. Care, "A local lattice Boltzmann method for multiple immiscible fluids and dense suspensions of drops," Phil. Trans. R. Soc. London, Ser. A **369**, 2255 (2011).

[29] M. R. Swift, E. Orlandini, W. R. Osborn, and J. M. Yeomans, "Lattice Boltzmann simulations of liquid-gas and binary fluid systems," Phys. Rev. E **54**, 5041 (1996).

[30] X. He, S. Chen, and R. Zhang, "A lattice Boltzmann scheme for incompressible multiphase flow and its application in simulation of Rayleigh-Taylor instability," J. Comput. Phys. **152**, 642 (1999).

[31] S. O. Unverdi and G. Tryggvason, "A front-tracking method for viscous, incompressible, multi-fluid flows," J. Comput. Phys. **100**, 25 (1992).

[32] G. Tryggvason, B. Bunner, A. Esmaeeli, D. Juric, N. Al-Rawahi, W. Tauber, J. Han, S. Nas, and Y.-J. Jan, "A front-tracking method for the computations of multiphase flow," J. Comput. Phys. **169**, 708 (2001).

[33] M. F. Tome and S. McKee, "GENSMAC: A computational marker and cell methods for free surface flows in general domains," J. Comput. Phys. **110**, 171 (1994).

[34] M. Dijkhuizen, I. Roghair, M. Van Sint Annaland, and J. A. M. Kuipers, "DNS of gas bubbles behaviour using an improved 3D front tracking model: Model development," Chem. Eng. Sci. **65**, 1427 (2010).

[35] C. M. Pooley and K. Furtado, "Eliminating spurious velocities in the free-energy lattice Boltzmann method," Phys. Rev. E **77**, 046702 (2008).

[36] S. Chen and G. D. Doolen, "Lattice Boltzmann method for fluid flows," Annu. Rev. Fluid Mech. **30**, 329 (1998).

[37] R. Clift, J. R. Grace, and M. E. Weber, *Bubbles, Drops, and Particles* (Academic Press, New York, 1978).

[38] P. Yue, J. J. Feng, C. Liu, and J. Shen, "A diffuse-interface method for simulating two-phase flows of complex fluids," J. Fluid Mech. **515**, 293 (2004).

[39] H. Ding, P. D. M. Spelt, and C. Shu, "Diffuse interface model for incompressible two-phase flows with large density ratios," J. Comput. Phys. **226**, 2078 (2007).

[40] O. Penrose and P. C. Fife, "Thermodynamically consistent models of phase-field type for the kinetics of phase transitions," Physica D **43**, 44 (1990).

[41] J. W. Cahn and J. E. Hilliard, "Free energy of a nonuniform system. I. Interfacial free energy," J. Chem. Phys. **28**, 258 (1958).

[42] J. W. Cahn and J. E. Hilliard, "Free energy of a nonuniform system. III. Nucleation in a two-component incompressible fluid," J. Chem. Phys. **31**, 688 (1959).

[43] A. J. Bray, "Theory of phase-ordering kinetics," Adv. Phys. **43**, 357 (1994).

[44] V. M. Kendon, M. E. Cates, I. Pagonabarraga, J.-C. Desplat, and P. Bladon, "Inertial effects in three-dimensional spinodal decomposition of a symmetric binary fluid mixture: A lattice Boltzmann study," J. Fluid Mech. **440**, 147 (2001).

[45] *Non-Equilibrium Thermodynamics*, edited by S. R. De Groot and P. Mazur (Dover Publications, New York, 1984).

[46] I. Ginzburg, F. Verhaeghe, and D. d'Humieres, "Two-relaxation-time lattice Boltzmann scheme: About parametrization, velocity, pressure and mixed boundary conditions," Comm. Comp. Phys. **3**, 427 (2008).

[47] H. Kusumaatmaja, "Lattice Boltzmann studies of wetting and spreading on patterned surfaces," Ph.D. dissertation (University of Oxford, 2008).

[48] J. C. Lee, *Thermal Physics: Entropy and Free Energies* (World Scientific, River Edge, NJ, 2002).

[49] R. G. M. Sman and S. Graaf, "Emulsion droplet deformation and breakup with Lattice Boltzmann model," Comput. Phys. Commun. **178**, 492 (2008).

[50] A. Mussa, P. Asinari, and L.-S. Luo, "Lattice Boltzmann simulations of 2D laminar flows past two tandem cylinders," J. Comput. Phys. **228**, 983 (2009).

[51] N. K. Ahmed and M. Hecht, "A boundary condition with adjustable slip length for lattice Boltzmann simulations," J. Stat. Mech. **2009**, P09017.

[52] H. Rusche, "Computational fluid dynamics of dispersed two-phase flows at high phase fractions," Ph.D. dissertation (Imperial College of Science, Technology & Medicine, 2002).

[53] P. L. Bhatnagar, E. P. Gross, and M. Krook, "A model for collision processes in gases. I. Small amplitude processes in charged and neutral one-component systems," Phys. Rev. **94**, 511 (1954).

[54] R. G. M. van der Sman, "Galilean invariant lattice Boltzmann scheme for natural convection on square and rectangular lattices," Phys. Rev. E **74**, 026705 (2006).

[55] I. Ginzburg, "Truncation errors, exact and heuristic stability analysis of two-relaxation-times lattice Boltzmann schemes for anisotropic advection-diffusion equation," Commun. Comput. Phys. **11**, 1439 (2012).

[56] R. Mei, L.-S. Luo, P. Lallemand, and D. d'Humieres, "Consistent initial conditions for lattice Boltzmann simulations," Comput. Fluids **35**, 855 (2006).

[57] E. Michaelides, *Particles, Bubbles & Drops: Their Motion, Heat and Mass Transfer* (World Scientific, Hackensack, NJ, 2006).

[58] D. d'Humieres, I. Ginzburg, M. Krafczyk, P. Lallemand, and L.-S. Luo, "Multiple-relaxation-time lattice Boltzmann models in three dimensions," Philos. Trans. R. Soc. London, Ser. A **360**, 437 (2002).